Systematic studies of elliptic flow measurements in Au + Au collisions at $\sqrt{s_{NN}} = 200$ GeV

S. Afanasiev,[17] C. Aidala,[7] N. N. Ajitanand,[44] Y. Akiba,[38,39] J. Alexander,[44] A. Al-Jamel,[34] K. Aoki,[23,38] L. Aphecetche,[46] R. Armendariz,[34] S. H. Aronson,[3] R. Averbeck,[45] T. C. Awes,[35] B. Azmoun,[3] V. Babintsev,[14] A. Baldisseri,[8] K. N. Barish,[4] P. D. Barnes,[26] B. Bassalleck,[33] S. Bathe,[4] S. Batsouli,[7] V. Baublis,[37] F. Bauer,[4] A. Bazilevsky,[3] S. Belikov,[3,16,*] R. Bennett,[45] Y. Berdnikov,[41] M. T. Bjorndal,[7] J. G. Boissevain,[26] H. Borel,[8] K. Boyle,[45] M. L. Brooks,[26] D. S. Brown,[34] D. Bucher,[30] H. Buesching,[3] V. Bumazhnov,[14] G. Bunce,[3,39] J. M. Burward-Hoy,[26] S. Butsyk,[45] S. Campbell,[45] J.-S. Chai,[18] S. Chernichenko,[14] J. Chiba,[19] C. Y. Chi,[7] M. Chiu,[7] I. J. Choi,[53] T. Chujo,[50] V. Cianciolo,[35] C. R. Cleven,[12] Y. Cobigo,[8] B. A. Cole,[7] M. P. Comets,[36] P. Constantin,[16] M. Csanád,[10] T. Csörgő,[20] T. Dahms,[45] K. Das,[11] G. David,[3] H. Delagrange,[46] A. Denisov,[14] D. d'Enterria,[7] A. Deshpande,[39,45] E. J. Desmond,[3] O. Dietzsch,[42] A. Dion,[45] J. L. Drachenberg,[1] O. Drapier,[24] A. Drees,[45] A. K. Dubey,[52] A. Durum,[14] V. Dzhordzhadze,[47] Y. V. Efremenko,[35] J. Egdemir,[45] A. Enokizono,[13] H. En'yo,[38,39] B. Espagnon,[36] S. Esumi,[49] D. E. Fields,[33,39] F. Fleuret,[24] S. L. Fokin,[22] B. Forestier,[27] Z. Fraenkel,[52,*] J. E. Frantz,[7] A. Franz,[3] A. D. Frawley,[11] Y. Fukao,[23,38] S.-Y. Fung,[4] S. Gadrat,[27] F. Gastineau,[46] M. Germain,[46] A. Glenn,[47] M. Gonin,[24] J. Gosset,[8] Y. Goto,[38,39] R. Granier de Cassagnac,[24] N. Grau,[16] S. V. Greene,[50] M. Grosse Perdekamp,[15,39] T. Gunji,[5] H.-Å. Gustafsson,[28] T. Hachiya,[13,38] A. Hadj Henni,[46] J. S. Haggerty,[3] M. N. Hagiwara,[1] H. Hamagaki,[5] H. Harada,[13] E. P. Hartouni,[25] K. Haruna,[13] M. Harvey,[3] E. Haslum,[28] K. Hasuko,[38] R. Hayano,[5] M. Heffner,[25] T. K. Hemmick,[45] J. M. Heuser,[38] X. He,[12] H. Hiejima,[15] J. C. Hill,[16] R. Hobbs,[33] M. Holmes,[50] W. Holzmann,[44] K. Homma,[13] B. Hong,[21] T. Horaguchi,[38,48] M. G. Hur,[18] T. Ichihara,[38,39] K. Imai,[23,38] M. Inaba,[49] D. Isenhower,[1] L. Isenhower,[1] M. Ishihara,[38] T. Isobe,[5] M. Issah,[44] A. Isupov,[17] B. V. Jacak,[45,†] J. Jia,[7] J. Jin,[7] O. Jinnouchi,[39] B. M. Johnson,[3] K. S. Joo,[31] D. Jouan,[36] F. Kajihara,[5,38] S. Kametani,[5,51] N. Kamihara,[38,48] M. Kaneta,[39] J. H. Kang,[53] T. Kawagishi,[49] A. V. Kazantsev,[22] S. Kelly,[6] A. Khanzadeev,[37] D. J. Kim,[53] E. Kim,[43] Y.-S. Kim,[18] E. Kinney,[6] A. Kiss,[10] E. Kistenev,[3] A. Kiyomichi,[38] C. Klein-Boesing,[30] L. Kochenda,[37] V. Kochetkov,[14] B. Komkov,[37] M. Konno,[49] D. Kotchetkov,[4] A. Kozlov,[52] P. J. Kroon,[3] G. J. Kunde,[26] N. Kurihara,[5] K. Kurita,[38,40] M. J. Kweon,[21] Y. Kwon,[53] G. S. Kyle,[34] R. Lacey,[44] J. G. Lajoie,[16] A. Lebedev,[16] Y. Le Bornec,[36] S. Leckey,[45] D. M. Lee,[26] M. K. Lee,[53] M. J. Leitch,[26] M. A. L. Leite,[42] H. Lim,[43] A. Litvinenko,[17] M. X. Liu,[26] X. H. Li,[4] C. F. Maguire,[50] Y. I. Makdisi,[3] A. Malakhov,[17] M. D. Malik,[33] V. I. Manko,[22] H. Masui,[49] F. Matathias,[45] M. C. McCain,[15] P. L. McGaughey,[26] Y. Miake,[49] A. Mignerey,[29] T. E. Miller,[50] A. Milov,[45] S. Mioduszewski,[3] G. C. Mishra,[12] J. T. Mitchell,[3] D. P. Morrison,[3] J. M. Moss,[26] T. V. Moukhanova,[22] D. Mukhopadhyay,[50] J. Murata,[38,40] S. Nagamiya,[19] Y. Nagata,[49] J. L. Nagle,[6] M. Naglis,[52] T. Nakamura,[13] J. Newby,[25] M. Nguyen,[45] B. E. Norman,[26] R. Nouicer,[3] A. S. Nyanin,[22] J. Nystrand,[28] E. O'Brien,[3] C. A. Ogilvie,[16] H. Ohnishi,[38] I. D. Ojha,[50] H. Okada,[23,38] K. Okada,[39] O. O. Omiwade,[1] A. Oskarsson,[28] I. Otterlund,[28] K. Ozawa,[5] R. Pak,[3] D. Pal,[50] A. P. T. Palounek,[26] V. Pantuev,[45] V. Papavassiliou,[34] J. Park,[43] W. J. Park,[21] S. F. Pate,[34] H. Pei,[16] J.-C. Peng,[15] H. Pereira,[8] V. Peresedov,[17] D. Yu. Peressounko,[22] C. Pinkenburg,[3] R. P. Pisani,[3] M. L. Purschke,[3] A. K. Purwar,[45] H. Qu,[12] J. Rak,[16] I. Ravinovich,[52] K. F. Read,[35,47] M. Reuter,[45] K. Reygers,[30] V. Riabov,[37] Y. Riabov,[37] G. Roche,[27] A. Romana,[24,*] M. Rosati,[16] S. S. E. Rosendahl,[28] P. Rosnet,[27] P. Rukoyatkin,[17] V. L. Rykov,[38] S. S. Ryu,[53] B. Sahlmueller,[30] N. Saito,[23,38,39] T. Sakaguchi,[5,51] S. Sakai,[49] V. Samsonov,[37] H. D. Sato,[23,38] S. Sato,[3,19,49] S. Sawada,[19] V. Semenov,[14] R. Seto,[4] D. Sharma,[52] T. K. Shea,[3] I. Shein,[14] T.-A. Shibata,[38,48] K. Shigaki,[13] M. Shimomura,[49] T. Shohjoh,[49] K. Shoji,[23,38] A. Sickles,[45] C. L. Silva,[42] D. Silvermyr,[35] K. S. Sim,[21] C. P. Singh,[2] V. Singh,[2] S. Skutnik,[16] W. C. Smith,[1] A. Soldatov,[14] R. A. Soltz,[25] W. E. Sondheim,[26] S. P. Sorensen,[47] I. V. Sourikova,[3] F. Staley,[8] P. W. Stankus,[35] E. Stenlund,[28] M. Stepanov,[34] A. Ster,[20] S. P. Stoll,[3] T. Sugitate,[13] C. Suire,[36] J. P. Sullivan,[26] J. Sziklai,[20] T. Tabaru,[39] S. Takagi,[49] E. M. Takagui,[42] A. Taketani,[38,39] K. H. Tanaka,[19] Y. Tanaka,[32] K. Tanida,[38,39] M. J. Tannenbaum,[3] A. Taranenko,[44] P. Tarján,[9] T. L. Thomas,[33] M. Togawa,[23,38] J. Tojo,[38] H. Torii,[38] R. S. Towell,[1] V.-N. Tram,[24] I. Tserruya,[52] Y. Tsuchimoto,[13,38] S. K. Tuli,[2] H. Tydesjö,[28] N. Tyurin,[14] C. Vale,[16] H. Valle,[50] H. W. van Hecke,[26] J. Velkovska,[50] R. Vertesi,[9] A. A. Vinogradov,[22] E. Vznuzdaev,[37] M. Wagner,[23,38] X. R. Wang,[34] Y. Watanabe,[38,39] J. Wessels,[30] S. N. White,[3] N. Willis,[36] D. Winter,[7] C. L. Woody,[3] M. Wysocki,[6] W. Xie,[4,39] A. Yanovich,[14] S. Yokkaichi,[38,39] G. R. Young,[35] I. Younus,[33] I. E. Yushmanov,[22] W. A. Zajc,[7] O. Zaudtke,[30] C. Zhang,[7] J. Zimányi,[20,*] and L. Zolin[17]

(PHENIX Collaboration)

[1]*Abilene Christian University, Abilene, Texas 79699, USA*

[2]*Department of Physics, Banaras Hindu University, Varanasi 221005, India*

[3]*Brookhaven National Laboratory, Upton, New York 11973-5000, USA*

[4]*University of California–Riverside, Riverside, California 92521, USA*

[5]*Center for Nuclear Study, Graduate School of Science, University of Tokyo, 7-3-1 Hongo, Bunkyo, Tokyo 113-0033, Japan*

[6]*University of Colorado, Boulder, Colorado 80309, USA*

[7]*Columbia University, New York, New York 10027 and Nevis Laboratories, Irvington, New York 10533, USA*

[8]*Dapnia, CEA Saclay, F-91191, Gif-sur-Yvette, France*

[9]*Debrecen University, H-4010 Debrecen, Egyetem tér 1, Hungary*

[10]*ELTE, Eötvös Loránd University, H-1117 Budapest, Pázmány P.s. 1/A, Hungary*

[11]*Florida State University, Tallahassee, Florida 32306, USA*

[12]*Georgia State University, Atlanta, Georgia 30303, USA*

[13]*Hiroshima University, Kagamiyama, Higashi-Hiroshima 739-8526, Japan*

[14]IHEP Protvino, State Research Center of Russian Federation, Institute for High Energy Physics, Protvino, RU-142281, Russia
[15]University of Illinois at Urbana-Champaign, Urbana, Illinois 61801, USA
[16]Iowa State University, Ames, Iowa 50011, USA
[17]Joint Institute for Nuclear Research, Moscow Region, RU-141980 Dubna, Russia
[18]KAERI, Cyclotron Application Laboratory, Seoul, Korea
[19]KEK, High Energy Accelerator Research Organization, Tsukuba, Ibaraki 305-0801, Japan
[20]KFKI Research Institute for Particle and Nuclear Physics of the Hungarian Academy of Sciences (MTA KFKI RMKI), H-1525 Budapest 114, P. O. Box 49, Budapest, Hungary
[21]Korea University, Seoul, 136-701, Korea
[22]Russian Research Center "Kurchatov Institute," Moscow, Russia
[23]Kyoto University, Kyoto 606-8502, Japan
[24]Laboratoire Leprince-Ringuet, Ecole Polytechnique, CNRS-IN2P3, Route de Saclay, F-91128, Palaiseau, France
[25]Lawrence Livermore National Laboratory, Livermore, California 94550, USA
[26]Los Alamos National Laboratory, Los Alamos, New Mexico 87545, USA
[27]LPC, Université Blaise Pascal, CNRS-IN2P3, Clermont-Fd, F-63177 Aubiere Cedex, France
[28]Department of Physics, Lund University, Box 118, SE-22100 Lund, Sweden
[29]University of Maryland, College Park, Maryland 20742, USA
[30]Institut für Kernphysik, University of Muenster, D-48149 Muenster, Germany
[31]Myongji University, Yongin, Kyonggido 449-728, Korea
[32]Nagasaki Institute of Applied Science, Nagasaki-shi, Nagasaki 851-0193, Japan
[33]University of New Mexico, Albuquerque, New Mexico 87131, USA
[34]New Mexico State University, Las Cruces, New Mexico 88003, USA
[35]Oak Ridge National Laboratory, Oak Ridge, Tennessee 37831, USA
[36]IPN-Orsay, Universite Paris Sud, CNRS-IN2P3, BP1, F-91406, Orsay, France
[37]PNPI, Petersburg Nuclear Physics Institute, Gatchina, Leningrad region, RU-188300, Russia
[38]RIKEN Nishina Center for Accelerator-Based Science, Wako, Saitama 351-0198, Japan
[39]RIKEN BNL Research Center, Brookhaven National Laboratory, Upton, New York 11973, USA
[40]Physics Department, Rikkyo University, 3-34-1 Nishi-Ikebukuro, Toshima, Tokyo 171-8501, Japan
[41]St. Petersburg State Polytechnic University, St. Petersburg, Russia
[42]Universidade de São Paulo, Instituto de Física, Caixa Postal 66318, São Paulo CEP05315-970, Brazil
[43]System Electronics Laboratory, Seoul National University, Seoul, Korea
[44]Chemistry Department, Stony Brook University, SUNY, Stony Brook, New York 11794, USA
[45]Department of Physics and Astronomy, Stony Brook University, SUNY, Stony Brook, New York 11794, USA
[46]SUBATECH (Ecole des Mines de Nantes, CNRS-IN2P3, Université de Nantes) BP 20722, F-44307, Nantes, France
[47]University of Tennessee, Knoxville, Tennessee 37996, USA
[48]Department of Physics, Tokyo Institute of Technology, Oh-okayama, Meguro, Tokyo 152-8551, Japan
[49]Institute of Physics, University of Tsukuba, Tsukuba, Ibaraki 305, Japan
[50]Vanderbilt University, Nashville, Tennessee 37235, USA
[51]Waseda University, Advanced Research Institute for Science and Engineering, 17 Kikui-cho, Shinjuku-ku, Tokyo 162-0044, Japan
[52]Weizmann Institute, Rehovot 76100, Israel
[53]Yonsei University, IPAP, Seoul 120-749, Korea
(Received 9 May 2009; published 31 August 2009)

We present inclusive charged hadron elliptic flow (v_2) measured over the pseudorapidity range $|\eta| < 0.35$ in Au + Au collisions at $\sqrt{s_{NN}} = 200$ GeV. Results for v_2 are presented over a broad range of transverse momentum ($p_T = 0.2$–8.0 GeV/c) and centrality (0–60%). To study nonflow effects that are correlations other than collective flow, as well as the fluctuations of v_2, we compare two different analysis methods: (1) the event-plane method from two independent subdetectors at forward ($|\eta| = 3.1$–3.9) and beam ($|\eta| > 6.5$) pseudorapidities and (2) the two-particle cumulant method extracted using correlations between particles detected at midrapidity. The two event-plane results are consistent within systematic uncertainties over the measured p_T and in centrality 0–40%. There is at most a 20% difference in the v_2 between the two event-plane methods in peripheral (40–60%) collisions. The comparisons between the two-particle cumulant results and the standard event-plane measurements are discussed.

DOI: 10.1103/PhysRevC.80.024909 PACS number(s): 25.75.Ld

I. INTRODUCTION

Collisions of Au + Au nuclei at the BNL Relativistic Heavy Ion Collider (RHIC) produce matter at very high energy density [1–4]. The dynamical evolution of this hot and dense

*Deceased.
†PHENIX spokesperson: jacak@skipper.physics.sunysb.edu

medium reflects its state and the degrees of freedom that govern the different stages it undergoes [5–7]. Azimuthal anisotropy measurements serve as a probe of the degree of thermalization, transport coefficients, and the equation of state (EOS) [8–10] of the produced medium.

Azimuthal correlations in Au + Au collisions at RHIC have been shown to consist of a mixture of jet and harmonic contributions [11–14]. Jet contributions are found to be relatively small for $p_T \lesssim 2.0$ GeV/c, with away-side jet yields strongly suppressed [13]. Significant modifications to the away-side jet topology have also been reported [15–17]. The harmonic contributions are typically characterized by the Fourier coefficients,

$$v_n = \langle \cos (n[\phi - \Psi_{\mathrm{RP}}]) \rangle \quad (n = 1, 2, \ldots), \tag{1}$$

where ϕ represents the azimuthal emission angle of a charged hadron and Ψ_{RP} is the azimuth of the reaction plane defined as containing both the direction of the impact parameter vector and the beam axis. The brackets denote statistical averaging over particles and events. The first two harmonics v_1 and v_2 are referred to as directed and elliptic flow, respectively.

It has been found that at low $p_T (p_T \lesssim 2.0$ GeV/c), the magnitude and trends of v_2 are underpredicted by hadronic cascade models supplemented with string dynamics [18], but they are well reproduced by models that either incorporate hydrodynamic flow [7,9] with a first-order phase transition and rapid thermalization, $\tau \sim 1$ fm/c [19], or use a quasiparticle ansatz but include more than just 2-to-2 interactions [20].

The mass dependence of v_2 as a function of p_T has been studied using identified baryons and mesons [19,21] and empirical scaling of elliptic flow per constituent quark was observed when the signal and the p_T of the hadron were divided by the number of constituent quarks $n_q (n_q = 2$ for mesons, 3 for baryons). This scaling is most clearly observed by plotting the data as a function of transverse kinetic energy $\mathrm{KE}_T \equiv m_T - m = \sqrt{p_T^2 + m^2} - m$ [22], where m_T and m denote the transverse mass and mass of the particle, respectively. A recent study [23] finds that the constituent quark scaling holds up to $\mathrm{KE}_T \approx 1$ GeV. This indicates partonic, rather than hadronic, flow and suggests that the bulk matter collectivity develops before hadronization takes place [24–26]. Results for the v_2 of the ϕ meson further validate the observation of partonic collectivity. The ϕ is not expected to be affected by hadronic interactions in the late stages of the medium evolution because of to its small interaction cross section with nonstrange hadrons [27].

All of the v_2 measurements referenced above were performed using the event-plane method [28]. In PHENIX studies, the event plane was determined at forward and backward pseudorapidities ($|\eta| = 3.1$–3.9) with the assumption that correlations induced by elliptic flow dominate over all other nonflow correlations [19]. Nonflow correlations are those that are not correlated with the reaction plane. Common sources of nonflow correlations include jets, the near-side ridge, quantum correlations, and resonance decays. Simulation studies [19,29] have shown that the correlations from jets and dijets become negligible when the rapidity separation between the particles and the event plane is greater than three units. Thus we expect that the event plane at forward pseudorapidities $|\eta| = 3.1$–3.9 in the PHENIX experiment would not have significant jet-correlation with particles measured within the PHENIX central arm spectrometer covering the pseudorapidity window $|\eta| < 0.35$. STAR and PHOBOS Collaborations have observed that in central Au + Au collisions, there is a ridge of particles [30,31] that are correlated in azimuthal angle with a high-p_T particle and that this ridge extends to $|\eta| < 4$ (for midrapidity triggers). The ridge could produce a nonflow correlation on which we can provide information by using our v_2 measurements, which are made with different techniques and at different rapidities.

Event-by-event flow fluctuations can also affect the magnitude of the extracted flow signal [32]. This occurs because the event plane at forward pseudorapidities is reconstructed using particles from participant nucleons whose positions fluctuate event-by-event. Assuming that v_2 fluctuates according to a Gaussian distribution, the v_2 fluctuation is proportional to the fluctuation of the initial geometry. This effect scales as $1/N_{\mathrm{part}}$, where N_{part} denotes the number of participant nucleons. The difference between v_2 values obtained from different methods can be quantitatively understood in terms of nonflow and fluctuation effects [33,34].

Hence in this paper we will compare the v_2 results from the event plane determined at two different pseudorapidities with the goal of investigating the sensitivity of v_2 to nonflow and fluctuation effects. Additionally, we will extract the elliptic flow with the two-particle cumulant method, which is expected to have higher sensitivity to nonflow contributions to v_2.

In this paper, we describe the PHENIX measurements of elliptic flow (v_2) at midrapidity ($|\eta| < 0.35$) in Au + Au collisions at $\sqrt{s_{NN}} = 200$ GeV obtained from a cumulant analysis of two-particle azimuthal correlations and the event-plane method over a broad range of $p_T (p_T = 0.2$–8 GeV/c) and centrality (0–60%). Section II describes the PHENIX apparatus, with an emphasis on the detectors relevant to the presented results, as well as the track selections used in the analysis. Section III gives details of the event-plane and cumulant methods as applied in PHENIX, and Sec. IV discusses their systematic uncertainties. The results from the two methods are reported in Sec. V. Section VI presents a comparison of v_2 results across different experiments and a discussion. The v_2 values obtained from the different methods are tabulated in the Appendix.

II. EXPERIMENTAL ANALYSIS

A. The PHENIX detector

The PHENIX detector consists of two central spectrometer arms at midrapidity that are designated East and West for their location relative to the interaction region, and two muon spectrometers at forward rapidity, similarly called North and South. A detailed description of the PHENIX detector can be found in Ref. [35]. The layout of the PHENIX detector during data taking in 2004 is shown in Fig. 1. Each central spectrometer arm covers a pseudorapidity range of $|\eta| < 0.35$ subtending 90° in azimuth and is designed to detect electrons, photons, and charged hadrons. Charged particles are tracked

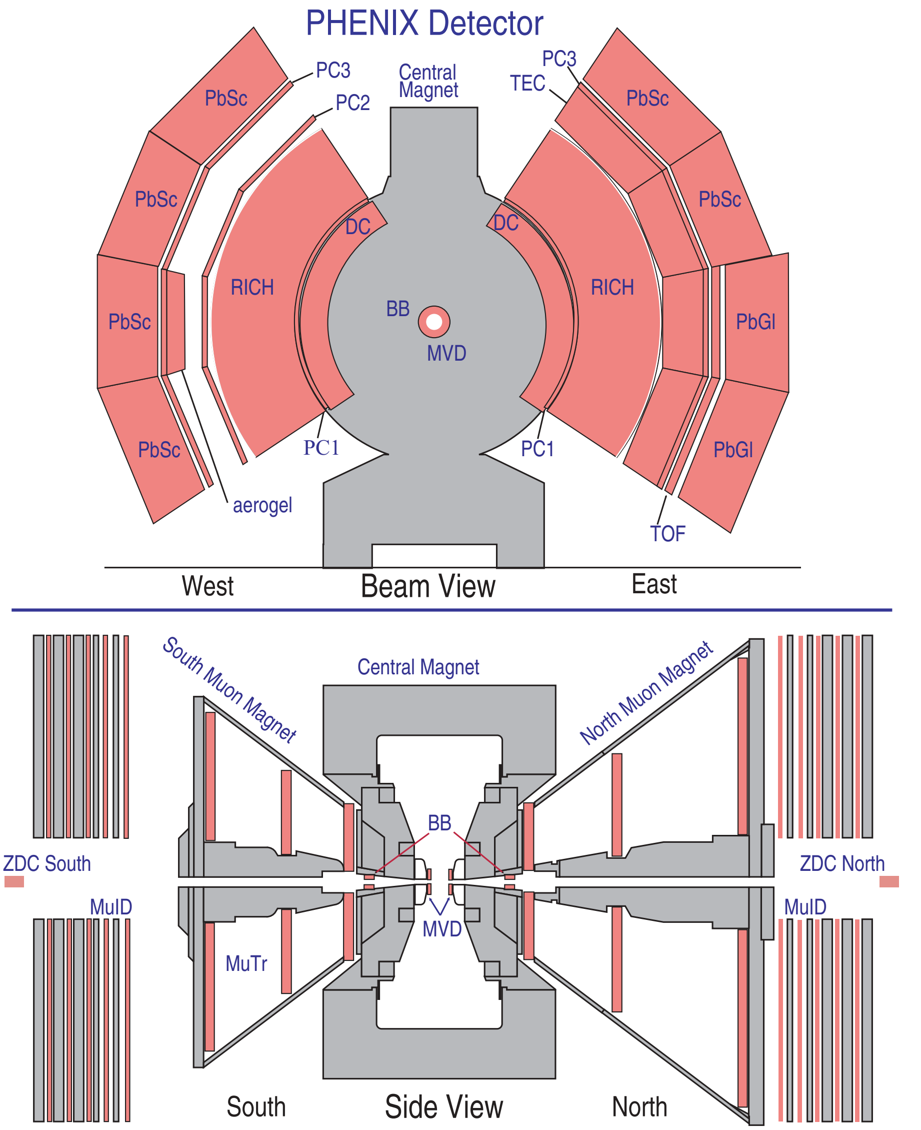

FIG. 1. (Color online) PHENIX experimental layout in 2004. Top: PHENIX central arm spectrometers viewed along the beam axis. Bottom: side view of the PHENIX muon arm spectrometers.

by drift chambers (DCs) positioned between 2.0 and 2.4 m radially outward from the beam axis and layers of multiwire proportional chambers with pad readout (two in the east arm and three in the west arm) PC1, PC2, and PC3 located at a radial distance of 2.4, 4.2, and 5 m, respectively. Particle identification is provided by ring imaging Čerenkov counters (RICHs), a time-of-flight scintillator wall (TOF), and two types of electromagnetic calorimeter (EMCAL), the lead scintillator (PbSc) and lead glass (PbGl).

The detectors used to characterize each event are the beam-beam counters (BBCs) [36] and the zero-degree calorimeters (ZDCs) [37]. These detectors are used to determine the time of the collision, the position of the collision vertex along the beam axis, and the collision centrality and also provide the event trigger. In this analysis the BBCs are also used to determine the event plane. Each BBC is composed of 64 elements, and a single BBC element consists of a 1 in. diameter mesh dynode photomultiplier tube (PMT) mounted on a 3 cm long quartz radiator. The BBCs are installed on the north and south sides of the collision point along the beam axis at a distance of 144 cm from the center of the interaction region and they surround the beam pipe. The BBC acceptance covers the pseudorapidity range $3.1 < |\eta| < 3.9$ and the full range of azimuthal angles.

The ZDCs are hadronic calorimeters located on both sides of the PHENIX detector. Each ZDC is mechanically subdivided into three identical modules of two interaction lengths. They cover a pseudorapidity range of $|\eta| > 6.5$ and measure the energy of the spectator neutrons with a 20 GeV energy resolution [37]. The shower maximum detectors (ZDC-SMDs) are scintillator strip hodoscopes between the first and second ZDC modules. This location approximately corresponds to the maximum of the hadronic shower. The horizontal coordinate is sampled by seven scintillator strips of 15 mm width, while the vertical coordinate is sampled by eight strips of 20 mm width. The active area of a ZDC-SMD is 105 mm $\times$ 110 mm (horizontal $\times$ vertical dimension). Scintillation light is delivered to a multichannel PMT M16 by wavelength-shifter fibers. The ZDC-SMD position resolution depends on the energy deposited in the scintillator. It varies from <3 mm, when the number of particles exceeds 100, to 10 mm for a smaller number of particles.

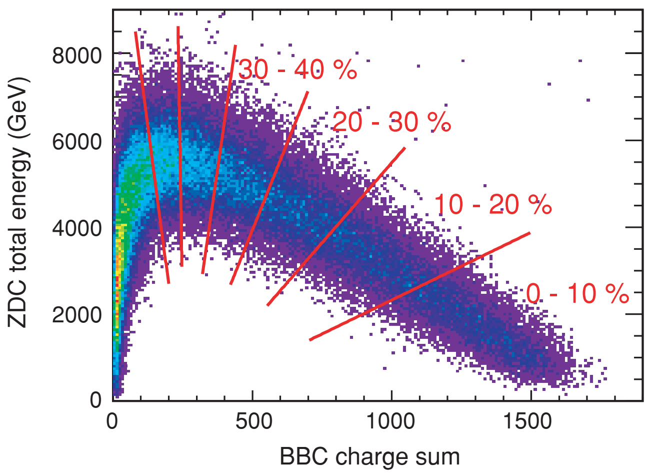

FIG. 2. (Color online) Correlation between ZDC energy and BBC charge sum for Au + Au collisions at $\sqrt{s_{NN}} = 200$ GeV. Solid lines represent the corresponding centrality boundaries up to 60% centrality bin.

B. Event selection

For the analyses presented here, we used approximately 850×10^6 minimum-bias triggered events. The minimum-bias trigger was defined by a coincidence between North and South BBC signals and an energy threshold of one neutron in the ZDCs. The events are selected offline to be within a z vertex of less than 30 cm from the nominal center of the PHENIX spectrometer. This selection corresponds to $92.2^{+2.5}_{-3.0}$% of the 6.9 b Au + Au inelastic cross section at $\sqrt{s_{NN}} = 200$ GeV [38]. The event centrality was determined by correlating the charge detected in the BBCs with the energy measured in the ZDCs, as shown in Fig. 2.

A Glauber model Monte Carlo simulation [39–41] that includes the responses of BBC and ZDC gives an estimate of the average number of participating nucleons $\langle N_{\mathrm{part}}\rangle$ for each centrality class. The simulation does not include fluctuations in the positions of the nucleons which give rise to eccentricity fluctuations. Table I lists the calculated values of $\langle N_{\mathrm{part}}\rangle$ for each centrality class.

TABLE I. Centrality classes and average number of participant nucleons $\langle N_{\mathrm{part}}\rangle$ obtained from a Glauber Monte Carlo simulation of the BBC and ZDC responses for Au + Au collision at $\sqrt{s_{NN}} = 200$ GeV. Each centrality class is expressed as a percentage of $\sigma_{\mathrm{AuAu}} = 6.9$ b inelastic cross section. Errors denote systematic uncertainties from the Glauber MC simulation.

Centrality	$\langle N_{\mathrm{part}}\rangle$
0–10%	325.2 ± 3.3
10–20%	234.6 ± 4.7
20–30%	166.6 ± 5.4
30–40%	114.2 ± 4.4
40–50%	74.4 ± 3.8
50–60%	45.5 ± 3.3

C. Track selection

Charged particle tracks are measured using information from the DC, the PC1 and PC3 detectors, and the z vertex from the BBC. The DC has 12 wire planes, which are spaced at 0.6 cm intervals along the radial direction from the beam axis. Each wire provides a track position measurement, with better than 150 μm spatial resolution in the azimuthal (ϕ) direction. The PC1 provides a space point in the ϕ and beam directions, albeit with lower resolution. This space point and the vertex position help determine the three-dimensional momentum vector by providing the polar angle for charged tracks at the exit of the DC. Trajectories are confirmed by requiring matching hits at PC3 to reduce secondary background. Tracks are then projected back to the collision vertex through the magnetic field to determine the momentum $\vec{p}$ [42]. The momentum resolution is $\delta p/p \simeq 0.7\% \oplus 1.0\% \times p$ (GeV/c). The momentum scale is known to 0.7%, as determined from the reconstructed proton mass using the TOF detector. Further details on track reconstruction and momentum determination can be found in Refs. [41,42].

The tracks reconstructed by the DC that do not originate from the event vertex have been investigated as potential background to the charged particle measurement. The main background sources include secondary particles from decays and e^+e^- pairs from the conversion of photons in the material between the vertex and the DC [41]. Tracks are required to have a hit in the PC3, as well as in the EMCAL, within at most 2σ of the expected hit location in both the azimuthal and beam directions. This cut reduces the background not originating in the direction of the vertex. To reduce the conversion background, we further require tracks to have $E/p_T > 0.2$, where E denotes the energy deposited in the EMCAL and p_T is the transverse momentum of particles measured in the DC. Since most of the electrons from photon conversion are genuine low p_T particles that were reconstructed as high p_T particles, requiring a large deposit of energy in the EMCAL suppresses the electron background [43]. We also require that there are no associated hits in the RICH. The RICH is filled with CO_2 gas at atmospheric pressure and has a charged particle threshold $\gamma_{\mathrm{th}} = 35$ to emit Čerenkov photons.

III. METHODS OF AZIMUTHAL ANISOTROPY MEASUREMENT

In this section, we introduce the methods for azimuthal anisotropy measurements as used in the PHENIX experiment. Section III A describes the event-plane method using the BBCs and ZDC-SMDs detectors, and Sec. III B describes the two-particle cumulant method.

A. Event-plane method

The event-plane method [28] uses the azimuthal anisotropy signal to estimate the angle of the reaction plane. The estimated reaction plane is called the "event plane" and is determined for each harmonic of the Fourier expansion of the azimuthal distribution. The event flow vector $\vec{Q}_n = (Q_x, Q_y)$ and azimuth of the event plane Ψ_n for the nth harmonic of the azimuthal anisotropy can be expressed as

$$Q_x \equiv |\vec{Q}_n| \cos(n\Psi_n) = \sum_i^M w_i \cos(n\phi_i), \tag{2}$$

$$Q_y \equiv |\vec{Q}_n| \sin(n\Psi_n) = \sum_i^M w_i \sin(n\phi_i), \tag{3}$$

$$\Psi_n = \frac{1}{n} \tan^{-1}\left(\frac{Q_y}{Q_x}\right), \tag{4}$$

where M denotes the number of particles used to determine the event plane, ϕ_i is the azimuthal angle of each particle, and w_i is the weight chosen to optimize the event-plane resolution. Once the event plane is determined, the elliptic flow v_2 can be extracted by correlating the azimuthal angle of emitted particles ϕ with the event plane, i.e.,

$$v_2 = \frac{v_2^{\mathrm{obs}}}{\mathrm{Res}\{\Psi_n\}} = \frac{\langle \cos(2[\phi - \Psi_n]) \rangle}{\langle \cos(2[\Psi_n - \Psi_{\mathrm{RP}}]) \rangle}, \tag{5}$$

where ϕ is the azimuthal angle of tracks in the laboratory frame, Ψ_n is the nth-order event plane, and the brackets denote an average over all charged tracks and events. The denominator Res $\{\Psi_n\}$ is the event-plane resolution that corrects for the difference between the estimated event plane Ψ_n and true reaction plane Ψ_{RP}.

In this paper, the second-harmonic event planes were independently determined with two BBCs located at the forward (BBC South, referred to as BBCS) and backward (BBC North, referred to as BBCN) pseudorapidities $|\eta| = 3.1$–3.9 [19]. The difference between the two independent event planes was used to estimate the event-plane resolution. The planes were also combined to determine the event plane for the full event. A large pseudorapidity gap between the charged particles detected in the central arms and the event plane at the BBCs reduces the effect of possible nonflow contributions, especially those from dijets [29]. The measured v_2 of hadrons in the central arms with respect to the combined second-harmonic BBC event plane will be denoted throughout this paper as $v_2\{\mathrm{BBC}\}$.

Two first-harmonic event planes were also determined using spectator neutrons at the two shower maximum detectors (ZDC-SMDs) that are sandwiched between the first and second modules of the ZDCs. Forward (ZDCS) and backward (ZDCN) SMDs which cover pseudorapidity $|\eta| > 6.5$ were used. The measured v_2 of hadrons in the central arms determined with respect to the first-harmonic ZDC-SMD event plane is denoted as $v_2\{\mathrm{ZDC\text{-}SMD}\}$.

The pseudorapidity gap between the hadrons measured in the central arms and the ZDC-SMDs is larger than that for the BBCs, which could cause a further reduction of nonflow contributions on $v_2\{\mathrm{ZDC\text{-}SMD}\}$. Since the ZDC-SMD measures spectator neutrons, the ZDC-SMD event plane should be insensitive to fluctuations in the participant event plane. Hence fluctuations in $v_2\{\mathrm{ZDC\text{-}SMD}\}$ should be suppressed up to fluctuations in the spectator positions.

For completeness, two further event planes are defined: (1) a combined event plane defined by the weighted average of event planes at the forward and backward pseudorapidities for both BBCs and ZDC-SMDs, and (2) an event plane found using tracks in the central arm. The event plane at the central arms (CNT) is only used to estimate the resolution of BBC and ZDC-SMD event planes by using a three-subevent combination of the ZDC-SMD, BBC, and CNT.

1. Event-plane determination

To determine an event plane, the contribution at each azimuthal angle needs to be appropriately weighted depending on the detector used. For the BBC, we chose the weights to be the number of particles detected in each phototube, while for the ZDC-SMD, the weights were based on the energy deposited in each of the SMD strips. For the CNT event plane, the weight was taken to be proportional to p_T up to 2 GeV/c and constant for $p_T > 2$ GeV/c. For the CNT event plane, we also adopted a unit weight ($w_i = 1$) and found that the resulting CNT event-plane resolution extracted by comparing the CNT event plane with the BBC and ZDC-SMD planes was nearly identical when using the p_T-dependent or unit weights.

Corrections were performed to remove possible biases from the finite acceptance of the BBC and ZDC-SMD. In this analysis, we applied two corrections called the recentering and shift methods [28]. In the recentering method, event flow vectors are shifted and normalized by using the mean $\langle Q \rangle$ and width σ of flow vectors, i.e.,

$$Q'_x = \frac{Q_x - \langle Q_x \rangle}{\sigma_x}, \quad Q'_y = \frac{Q_y - \langle Q_y \rangle}{\sigma_y}. \tag{6}$$

This correction reduces the dependence of the event-plane resolution on the laboratory angle. Most acceptance effects were removed by the application of the recentering method. However, remaining small corrections were applied after recentering using the shift method [28], in which the reaction plane is shifted by $\Delta\Psi_n$ defined by

$$n\Delta\Psi_n(\Psi_n) = \sum_{k=1}^{k_{\max}} \frac{2}{k}[-\langle \sin(kn\Psi_n) \rangle \cos(kn\Psi_n) + \langle \cos(kn\Psi_n) \rangle \sin(kn\Psi_n)], \tag{7}$$

where $k_{\max} = 8$ in this analysis. The shift ensures that $dN/d\Psi_n$ is isotropic. When $k_{\max}$ was reduced to $k_{\max} = 4$, the difference in the extracted v_2 was negligible, and thus we include no systematic uncertainty due to the choice of $k_{\max}$ in our v_2 results.

Independent corrections were applied to each centrality selection in 5% increments and in 20 cm steps in the z vertex to optimize the event-plane resolution. The corrections were also done for each experimental run (the duration of a run is typically 1–3 h) to minimize the possible time-dependent response of detectors.

Figure 3 shows event-plane distributions for a subsample of the entire data set. After all corrections are applied, the event-plane distributions are isotropic.

2. Event-plane resolution

The event-plane resolution for v_2 was evaluated by both the two-subevent and three-subevent methods. In the two-subevent

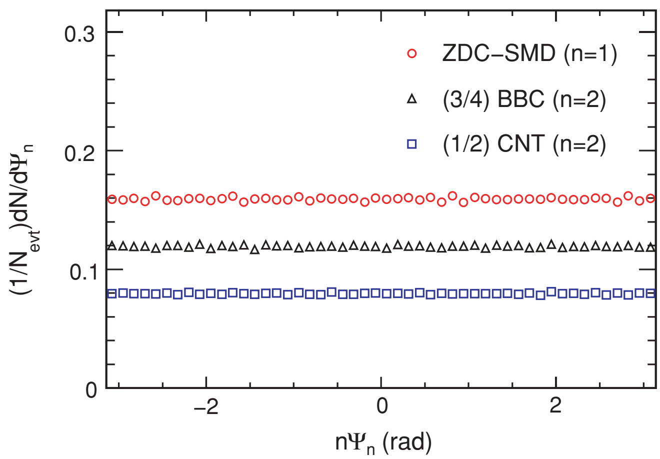

FIG. 3. (Color online) Event-plane distributions after applying all corrections for the ZDC-SMD, BBC, and CNT. The statistical error bars are smaller than the symbols. The distributions for the BBC and CNT event planes are scaled by 3/4 and 1/2 to improve visibility.

method, the event-plane resolution [28] is expressed as

$$\langle \cos(kn[\Psi_n - \Psi_{RP}])\rangle = \frac{\sqrt{\pi}}{2\sqrt{2}}\chi_n e^{-\chi_n^2/4}\left[I_{(k-1)/2}\left(\frac{\chi_n^2}{4}\right) + I_{(k+1)/2}\left(\frac{\chi_n^2}{4}\right)\right], \quad (8)$$

where $\chi_n = v_n\sqrt{2M}$, M is the number of particles used to determine the event plane Ψ_n, I_k is the modified Bessel function of the first kind, and $k = 1$ for the second-harmonic BBC event plane. For the ZDC-SMD event plane, the resolution is estimated with either $k = 1$ or 2 in Eq. (8). We will discuss the difference between these estimates in Sec. IV A.

To determine the event-plane resolution, we need to determine χ_n. Since the North and South BBCs have approximately the same η coverage, the event-plane resolution of each subdetector is expected to be the same. The same is true for the North and South ZDC-SMDs. Thus, the subevent resolution for South and North event planes can be expressed as

$$\langle \cos(2[\Psi_n^{S(N)} - \Psi_{RP}])\rangle = \sqrt{\langle \cos(2[\Psi_n^{S} - \Psi_n^{N}])\rangle}, \quad (9)$$

where $\Psi_n^{S(N)}$ denotes the event plane determined by the South (North) BBC or ZDC-SMD. Once the subevent resolution is obtained from Eq. (9), one can calculate χ_n^{sub} using Eq. (8). The χ_n for the full event can then be estimated by $\chi_n = \sqrt{2}\chi_n^{sub}$. This is then substituted into Eq. (8) to give the full-event resolution. Since the multiplicity of the full event is twice as large as that of the subevent, χ_n is proportional to $\sqrt{M}$.

In the three-subevent method, the resolution of each subevent is calculated by adding a reference event plane Ψ_n^C in Eq. (9):

$$\mathrm{Res}\{\Psi_l^A\} = \sqrt{\langle \cos(2[\Psi_l^A - \Psi_m^B])\rangle}\sqrt{\frac{\langle \cos(2[\Psi_n^C - \Psi_l^A])\rangle}{\langle \cos(2[\Psi_m^B - \Psi_n^C])\rangle}}, \quad (10)$$

where l, m, n are the harmonics of the event plane for subevents A, B, and C, respectively. The multiplicity of each subevent is not necessarily the same in Eq. (10).

The resolution of each subdetector for the BBC and ZDC-SMD can be evaluated with the three-subevent method. For the BBC event plane, the reference event plane is chosen to be the ZDC-SMD event plane and vice versa. We found that the agreement of the event-plane resolutions for BBCS and BBCN is much better than 1%, while the ZDCS and ZDCN resolutions agree within 2%.

Figure 4 shows the full-event resolution as a function of centrality. The resolution of ZDC-SMD is much smaller than that of BBC because the resolution of the first-harmonic event plane is proportional to $(\chi_1)^2$. The dashed lines are the resolutions obtained from the three-subevent method with the CNT event plane as the reference plane. For example, the BBC event-plane resolution is estimated by substituting $\Psi_l^A \to \Psi_2^{BBC}$, $\Psi_m^B \to \Psi_2^{CNT}$, and $\Psi_n^C \to \Psi_1^{ZDC-SMD}$ in Eq. (10). By including the CNT event plane, the BBC resolution increases by about 3% over that of the two-subevent method. For the ZDC-SMD, we observe the opposite effect, namely, the resolution decreases by about 8%. In Sec. VI, the resulting $v_2\{\mathrm{BBC}\}$ and $v_2\{\mathrm{ZDC\text{-}SMD}\}$, corrected by the resolution obtained using the ZDC-BBC-CNT combination, will be compared against those with the resolution determined from South-North subevents. Table II summarizes the event-plane resolutions.

3. *Correlation of event planes*

Figure 5 shows the correlation of two different event planes as a function of centrality. The first-harmonic event-plane correlation for South-North detector combinations is negative both for the ZDC-SMDs and the BBCs over all centrality bins, as shown in Fig. 5(a). This is because v_1 is an odd function of η. The magnitude of the ZDC-SMD correlation is about a factor of 2 larger than that of the BBCs for midcentral collisions. This indicates that the magnitude of v_1 and the subevent multiplicity

TABLE II. Event-plane resolutions for centrality 0–60% at $\sqrt{s_{NN}} = 200$ GeV. S-N denotes the resolutions estimated from South and North correlation of BBC and ZDC-SMD using Eqs. (8) and (9), and resolutions for ZDC-BBC-CNT are estimated from Eq. (10). The errors are statistical only.

Centrality	S-N	ZDC-BBC-CNT
	$\mathrm{Res}\{\Psi_2^{BBC}\}$	
0–10%	0.2637 ± 0.0003	0.272 ± 0.003
10–20%	0.3809 ± 0.0002	0.394 ± 0.001
20–30%	0.3990 ± 0.0002	0.4106 ± 0.0008
30–40%	0.3634 ± 0.0002	0.3759 ± 0.0007
40–50%	0.2943 ± 0.0003	0.3067 ± 0.0007
50–60%	0.2106 ± 0.0004	0.2240 ± 0.0009
	$\mathrm{Res}\{\Psi_1^{ZDC-SMD}\}$	
0–10%	0.02 ± 0.01	0.0223 ± 0.0003
10–20%	0.059 ± 0.003	0.0574 ± 0.0002
20–30%	0.087 ± 0.002	0.0818 ± 0.0002
30–40%	0.100 ± 0.002	0.0928 ± 0.0002
40–50%	0.102 ± 0.002	0.0920 ± 0.0002
50–60%	0.100 ± 0.002	0.0798 ± 0.0003

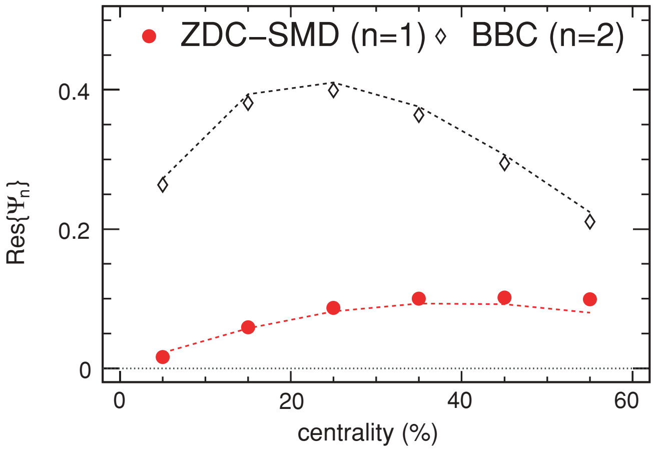

FIG. 4. (Color online) Full-event resolutions for the ZDC-SMD and BBC from the two-subevent method, Eq. (8), as a function of centrality in Au + Au at $\sqrt{s_{NN}} = 200$ GeV. The dashed lines represent resolutions from the three-subevent method with the CNT event plane as a reference. Statistical errors are smaller than the symbols.

at higher pseudorapidities are larger than those at the BBC location, since the magnitude of the correlation is proportional to $v_1^2 M$. Figure 5(b) shows the correlation of the first-harmonic event planes between BBC and ZDC-SMD. The same-side η correlation is negative, while the opposite-side η correlation is positive, which shows that the particles detected at the BBCs (dominantly charged pions emitted from participant nucleons) have the opposite sign of v_1 compared to the spectator neutrons detected at the ZDCs-SMDs.

The correlation of the mixed-harmonic event planes provides the sign of v_2, since the correlation is given by the expression [28]

$$\begin{aligned}
&\left\langle \cos\left(2\left[\Psi_1^{\mathrm{ZDC-SMD}} - \Psi_2^{\mathrm{BBC}}\right]\right)\right\rangle \\
&\quad\approx \frac{2}{\pi}\left(\mathrm{Res}\left\{\Psi_1^{\mathrm{ZDC-SMD}}\right\}\right)^2 \mathrm{Res}\left\{\Psi_2^{\mathrm{BBC}}\right\} \\
&\quad= \pm 2\sqrt{2}\frac{2}{\pi}\left\langle \cos\left(\Psi_1^{\mathrm{ZDCS}} - \Psi_1^{\mathrm{ZDCN}}\right)\right\rangle \\
&\qquad\times\sqrt{\left\langle \cos\left(2\left[\Psi_2^{\mathrm{BBCS}} - \Psi_2^{\mathrm{BBCN}}\right]\right)\right\rangle}. \qquad (11)
\end{aligned}$$

Three assumptions were made to obtain Eq. (11): (1) the BBC and ZDC-SMD are statistically independent, (2) the weak flow limit ($\chi_n \ll 1$) is applicable [28], and (3) the subevent multiplicity M is equal in the North-South direction for the same detector type. Thus the sign of the correlation of the mixed-harmonic event planes in Eq. (11) is determined by the term $\mathrm{Res}\{\Psi_2^{\mathrm{BBC}}\}$, which in turn determines the sign of v_2 measured at the BBC.

Figure 6 shows the mixed-harmonic correlation of the ZDC-SMD and BBC event planes as a function of centrality. The approximations in Eq. (11) provide a good description of the magnitude of the measured correlation as shown by the dashed line. The correlation is positive over all centrality bins. This result indicates that the sign of v_2 at the BBC is positive.

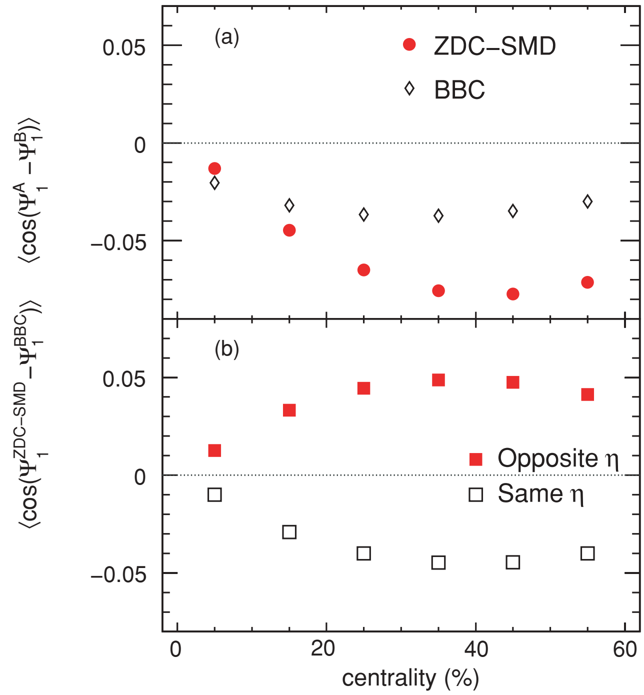

FIG. 5. (Color online) (a) Correlation of first-harmonic event planes between forward and backward ZDC-SMDs and BBCs as a function of centrality. (b) Correlation of first-harmonic event planes between ZDC-SMDs and BBCs as a function of centrality, for correlations of opposite- and same-side η subevents. Statistical errors are smaller than the symbols.

B. Cumulant method

In this section, we present the application of the cumulant method for azimuthal anisotropy measurements in PHENIX. This method uses cumulants of multiparticle correlations [44,45] to extract the azimuthal anisotropy. The cumulant method has been successfully applied in several heavy-ion experiments utilizing detectors with full azimuthal coverage (NA49, STAR) [46,47]. Here, we describe the first application

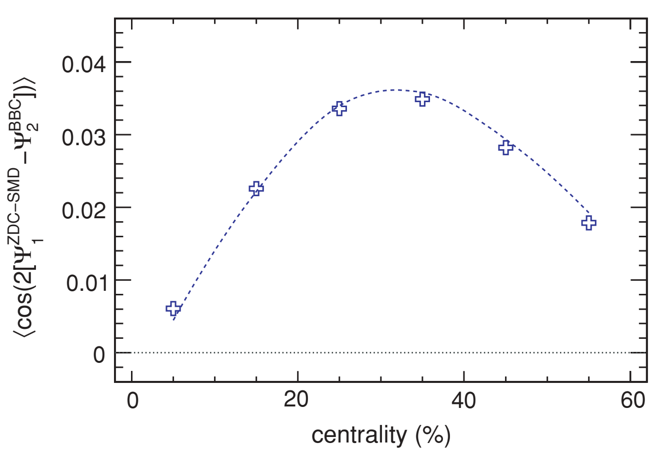

FIG. 6. (Color online) Correlation between the first-harmonic ZDC-SMD and the second-harmonic BBC event planes as a function of centrality. The dashed line shows the result obtained using Eq. (11). Statistical errors are smaller than the data symbols.

of the method for a detector with only partial azimuthal coverage. The cumulant method does not require the measurement of the reaction plane, instead the cumulants of multiparticle azimuthal correlations are related to the flow harmonics v_n, where n is the harmonic being evaluated. The cumulants can be constructed in increasing order according to the number of particles that are correlated with each other. Since PHENIX has partial azimuthal coverage, reliable extraction of azimuthal anisotropy requires the choice of a fixed number of particles from each event to avoid additional numerical errors [44].

Particles in an event are selected over a fixed (p_T,η) range where there is sufficient multiplicity. From this set, particles (called integral particles hereafter) are selected to determine the integrated flow, which is flow measured over a large (p_T,η) bin. This is done by excluding particles within small (p_T,η) bins from all available particles to avoid autocorrelations. The particles within a small (p_T,η) window (called differential particles hereafter) are used to determine the differential flow. For each event, a fixed number M of particles, chosen at random among the integral particles in the event, are used to reconstruct the integrated flow through the generating function $G_2(z)$ defined by

$$G_2(z) = \prod_{j=1}^{M}\left[1 + \frac{w_j}{M}(z^* e^{2i\phi_j} + ze^{-2i\phi_j})\right], \qquad (12)$$

where w_j is the weight, chosen to be equal to 1 in our analysis, ϕ_j is the azimuth of the detected particles, and M is the multiplicity chosen for the integrated flow reconstruction. $G_2(z)$ is a real-valued function of the complex variable z. The average of $G_2(z)$ over events is then expanded in a power series to generate multiparticle azimuthal correlations. The generating function of the cumulants, defined by

$$\mathcal{C}_2(z) \equiv M(\langle G_2(z)\rangle^{1/M} - 1), \qquad (13)$$

generates cumulants of azimuthal correlations to all orders, the lowest being the second order, as detailed in Sec. II B of Ref. [44]. The formulas used to compute the cumulants from which the v_2 is computed are given in Appendix B of Ref. [44]. In the case of a perfect acceptance, the relations between the anisotropy parameter v_2 and the lowest order cumulants are

$$v_2\{2\}^2 = c_2\{2\}, \qquad (14)$$
$$v_2\{4\}^4 = -c_2\{4\}, \qquad (15)$$

for the integrated anisotropy. Here $v_2\{2\}$ and $v_2\{4\}$ are the second- and fourth-order v_2, respectively; whereas, $c_2\{2\}$ and $c_2\{4\}$ are the second- and fourth-order cumulants. Because the typical multiplicity of charged hadrons in PHENIX, which is $\approx$40 for midcentral collisions, did not allow a reliable calculation of $v_2\{4\}$, we report here only the $v_2\{2\}$ results.

The remaining differential particles in the same event are selected in different (p_T,η) bins, and the differential cumulants are calculated from the generating function

$$\mathcal{D}_{2/2}(z) \equiv \frac{\langle e^{2i\psi} G_2(z)\rangle}{\langle G_2(z)\rangle}, \qquad (16)$$

where $\langle G(z)\rangle$ denotes an average over all events, and ψ is the azimuth of each differential particle. $D_{2/2}$ denotes the second-order differential cumulant computed with respect to the second-order integral cumulant.

The differential $v_{2/2}\{2\}(p_T,\eta)$, the second-order differential v_2 with respect to the second-order integrated v_2, is calculated from the relation

$$v_{2/2}\{2\}(p_T,\eta) = \frac{d_{2/2}\{2\}(p_T,\eta)}{v_2\{2\}}, \qquad (17)$$

where $d_{2/2}\{2\}(p_T,\eta)$ is the second-order differential cumulant. These relations have to be modified through acceptance corrections, which are detailed below.

1. Acceptance/efficiency corrections

The central arms detectors in PHENIX have only partial azimuthal coverage, and the implementation of the cumulant method requires an additional acceptance correction. To correct for the influence of the detector acceptance on the raw anisotropy values, we apply a correction factor using the prescription described in Ref. [44]. The acceptance and efficiency of the detector is characterized by a function $A(\phi, p_T,\eta)$, which is expressed in terms of the Fourier series as

$$A(\phi, p_T,\eta) = \sum_{p=-\infty}^{+\infty} a_p(p_T,\eta)e^{ip\phi}. \qquad (18)$$

The Fourier coefficients $a_p(p_T,\eta)$ for the detector acceptance were extracted from the fit of the respective azimuthal distributions of integral and differential particles. The coefficients resulting from such fits were then used to calculate the correction factor for the raw values of the v_2 following the procedure detailed in Appendix C of Ref. [44].

Figure 7 shows a typical azimuthal angular distribution of differential particles detected in the PHENIX central arms and the corresponding Fourier fit used to correct for acceptance inhomogeneities. The Fourier fit reproduces well the overall features of the acceptance profile. This produces typical correction factors, which are in the range 1.1–1.2 for the differential flow and depend very little on centrality and p_T, as shown in Fig. 8.

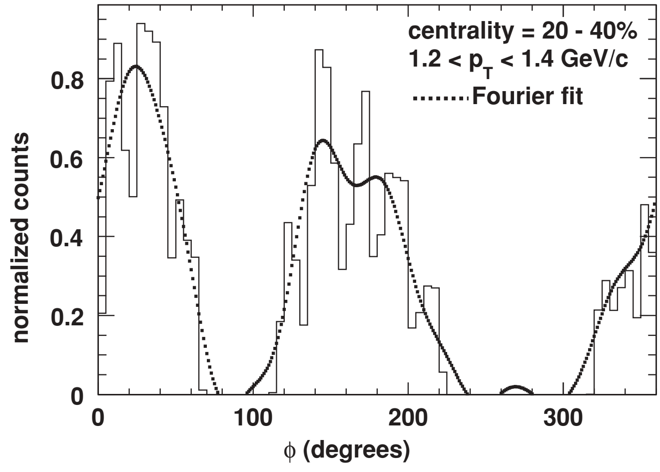

FIG. 7. Azimuthal angular distribution and corresponding Fourier fit for centrality 20–40% and $p_T = 1.2$–1.4 GeV/c.

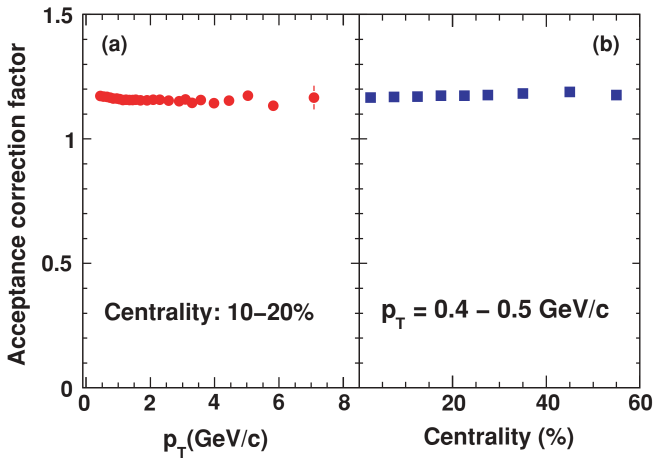

FIG. 8. (Color online) Acceptance correction factor for differential $v_2\{2\}$ as a function of (a) p_T for centrality 10–20% and (b) centrality for p_T range 0.4–0.5 GeV/c in Au + Au collisions at $\sqrt{s_{NN}} = 200$ GeV.

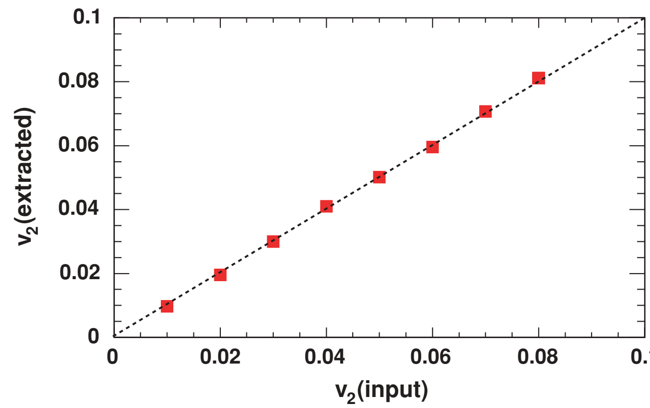

FIG. 9. (Color online) Comparison of input and extracted differential v_2 values for a fixed integrated v_2 of 8%. The dotted line indicates the expectation if input and reconstructed values are the same.

2. *Simulations*

While Fig. 7 shows that the uneven detector acceptance is reproduced by the Fourier fit, a better test of the cumulant method is to use Monte Carlo simulations, as in Ref. [44]. For these tests, events were generated with particles having a distribution of the form $1 + 2v_1 \cos\phi + 2v_2 \cos 2\phi$, with known integrated and differential azimuthal anisotropies. The anisotropy was introduced into the events by way of a Fourier weighted selection of the azimuthal angles followed by a random event rotation designed to simulate the random orientation of the reaction plane. The multiplicity of these events was chosen to reflect the typical multiplicity measured with the PHENIX detector, and the ϕ angles were chosen from a filter that is representative of the PHENIX acceptance. We extracted Fourier components from these simulated results and applied these to extract corrected elliptic flow values.

Figure 9 shows selected results from these simulations. Corrected differential anisotropy values are compared for various input differential v_2 values, with the integrated v_2 kept fixed. The dotted line shows the trend expected if the extracted v_2 is identical to the input value used to generate the events. The good agreement between the input and extracted v_2 attests to the reliability of the analysis method within the acceptance of the PHENIX central arms.

IV. SYSTEMATIC UNCERTAINTIES

In this section, we present the systematic uncertainties on the v_2 from the event-plane method (Sec. IV A) and the two-particle cumulant method (Sec. IV B). Table III lists the different sources of systematic errors for each method. The errors in Table III are categorized by type:

(i) point-to-point error uncorrelated between p_T bins,
(ii) p_T correlated, all points move in the same direction but not by the same factor,
(iii) an overall normalization error in which all points move by the same factor independent of p_T.

TABLE III. Systematic uncertainties given in percent on the v_2\{ZDC-SMD\}, v_2\{BBC\}, and $v_2\{2\}$ measurements. The ranges correspond to different systematic errors for different centrality bins.

Error source	Percentage error		Type
	v_2\{BBC\}	v_2\{ZDC-SMD\}	
Background contribution	<5% in p_T < 4 GeV/c		B
	5–30% in p_T > 4 GeV/c		B
Event-plane calibration	1–5%		C
Event-plane determination	1–4%	1–16%	C
Acceptance effect on event planes	1%	1–25%	C
	$v_2\{2\}$		
Fixed multiplicity	5%		B
Integrated p_T range	3–8%		B
Background correction	6–10%		B

A. Event-plane method

1. Background contributions

To study the influence of background on our results, we varied one of the track selections while keeping other cuts fixed and investigated the effect on v_2 in the following two cases: (i) the PC3 and EMCAL matching cuts, $\pm1.5\sigma$ and $\pm2.5\sigma$ matching cuts, and (ii) $E > 0.15p_T$ and $E > 0.25p_T$. For both conditions, we found that the difference of the v_2 is 1–2% for $p_T < 4$ GeV/c, and 5–20% for $p_T > 4$ GeV/c depending on p_T and centrality.

The effect of the RICH veto cut has also been studied. Since the contribution of charged π increases without the RICH veto cut, the p/π ratio decreases at high p_T. Thus, the v_2 for charged hadrons could be modified due to the difference of v_2 between protons and π in the range $4 < p_T < 8$ GeV/c. We found that v_2 is 10–20% different without the RICH veto cut for $p_T >$ 4–5 GeV/c, where the charged π starts firing the RICH.

One of the remaining sources of background contribution comes from the random tracks that are accidentally associated with the tracks in PC3. These random tracks have been estimated by swapping the z coordinate of the PC3 hits and then by associating those hits with the real tracks. Figure 10 shows the comparison of the radial PC3 matching distribution between the real and random tracks for $6 < p_T < 8$ GeV/c. The signal-to-background ratio S/B is evaluated in the $\sigma_{PC3} < 2$ window and is $\sim$52 for $6 < p_T < 8$ GeV/c in centrality 0–60%.

The ratio of real and random tracks with and without the $E/p_T > 0.2$ cut is shown as a function of p_T for centrality 0–60% in Fig. 11. The $E/p_T > 0.2$ cut reduces the random tracks and improves the S/B ratio by a factor of $\approx$10–24 for $p_T > 4$ GeV/c. Since random tracks are not expected to be correlated with the event plane, we assume that their $v_2 = 0$ and evaluate the systematic uncertainty on v_2 to be less than 2% for $p_T > 4$ GeV/c, increasing to 5% for $p_T < 0.5$ GeV/c.

There is a finite residual background contribution even after the $E/p_T > 0.2$ has been applied, as observed in Fig. 10. The residual backgrounds have been estimated by fitting the σ_{PC3} with a double Gaussian while requiring that the signal and residual background σ_{PC3} distribution have the same mean. For the highest p_T bin, we found that the signal-to-background ratio is $\sim$5 for $\sigma_{PC3} < 2$. The systematic error on v_2 is evaluated by comparing the measured v_2 with that of the signal

$$v_2^S = \left(1 + \frac{B}{S}\right) v_2 - \frac{B}{S} v_2^B, \tag{19}$$

where v_2^S, v_2^B and v_2 are, respectively, v_2 of signal, background estimated for $\sigma_{PC3} > 3$, and measured within the 2σ matching window. The systematic uncertainties are less than 5% for $p_T < 4$ GeV/c, and $\sim$5–10% for higher p_T. All the above systematic errors are added in quadrature, and the overall systematic error from the background contribution is estimated to vary from <5% for $p_T < 4$ GeV/c to $\sim$30% for higher p_T.

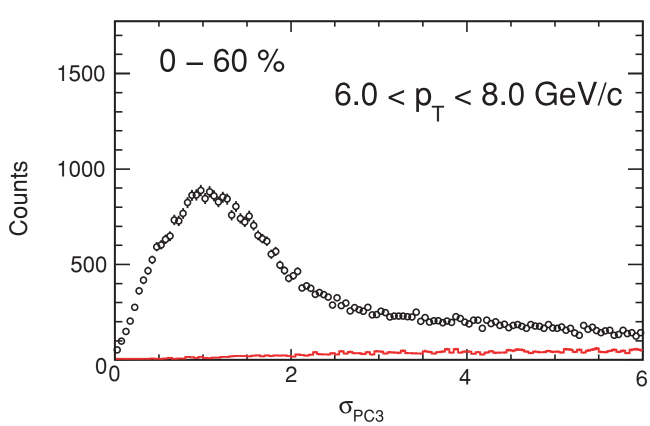

FIG. 10. (Color online) Radial PC3 matching distribution for real (open circles) and random (solid lines) tracks for $6 < p_T < 8$ GeV/c in centrality 0–60%.

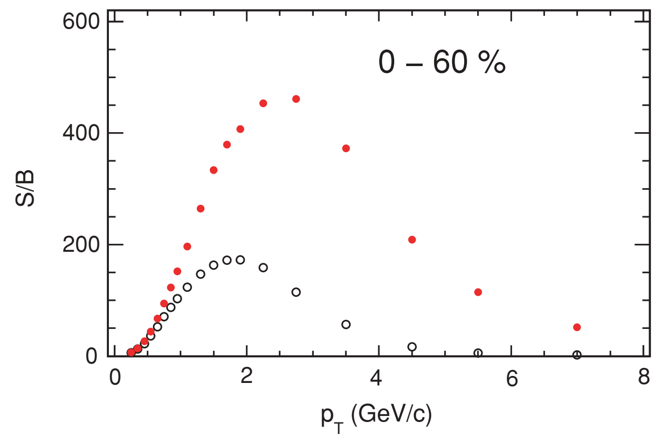

FIG. 11. (Color online) Ratio of real S to random B tracks as a function of p_T in centrality 0–60%. Solid and open circles show the S/B ratio with and without $E/p_T > 0.2$, respectively.

2. Event-plane calibrations

The procedures used in the determination and calibration of event planes are the dominant sources of systematic errors on v_2 and are discussed in the following sections.

Different calibration procedures of the BBC event plane were extensively studied for previous Au + Au data sets [19]. We followed the same procedure to study the systematic errors on the BBC and ZDC-SMD event planes. Systematic uncertainties from the shift methods on $v_2\{\text{BBC}\}$ are $\sim$1–5% depending on the centrality. The systematic errors on the $v_2\{\text{ZDC-SMD}\}$ are 1–2% larger than those on $v_2\{\text{BBC}\}$ for centrality 10–30% and 50–60%, although those are still less than 5%.

3. Event-plane determination

Figure 12 shows the comparison of $\langle v_2\rangle$ for different subdetectors with respect to the BBC and ZDC-SMD event planes as a function of centrality. Systematic errors are estimated by taking the maximum difference of the v_2 from the South and North event planes to that from the combined

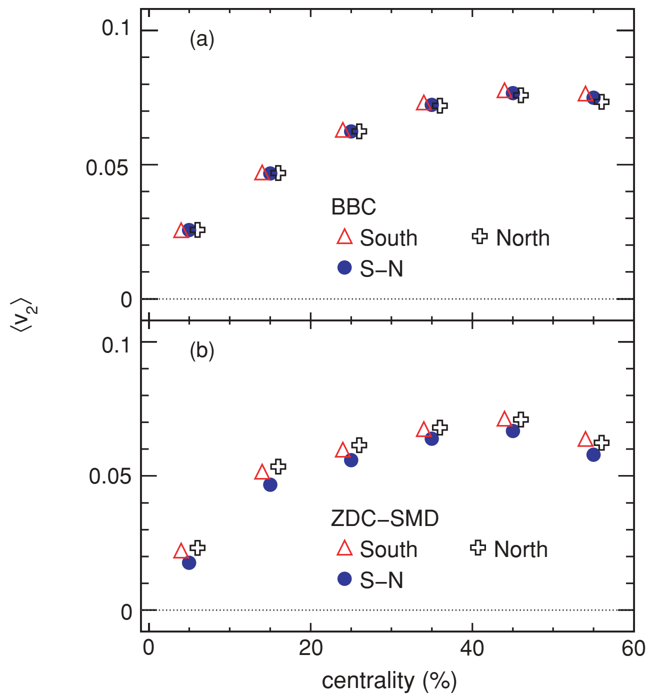

FIG. 12. (Color online) Comparison of $\langle v_2 \rangle$ averaged over $0.2 < p_T < 8$ GeV/c as a function of centrality for the (a) BBC and (b) ZDC-SMD event planes from South and North subdetectors and from combined South-North (S-N) event planes. Results from South and North event planes are shifted in the x direction to improve visibility. Only statistical errors are shown and they are smaller than the symbols.

South-North event plane scaled by $2/\sqrt{12}$ for each centrality. Systematic errors range from 1–4% for the BBC, and 1–16% for the ZDC-SMD event planes depending on the centrality bins.

4. Effect of nonuniform acceptance on v_2

In this subsection, we discuss the effect of nonuniform acceptance on the measured v_2. In practice, the imperfect azimuthal acceptance of the BBC or ZDC-SMD or the central arms could induce an azimuthal-dependent event-plane resolution and/or smear the magnitude of v_2. To study the possible effect of nonuniform acceptance, the measured v_2 is decomposed into X and Y components [48]:

$$\begin{aligned} v_2^{\mathrm{X}} &= \frac{\sqrt{2}}{a_4^{+}} \frac{\langle \cos(2\phi)\cos(2\Psi_n^{\mathrm{A}})\rangle}{\mathrm{Res}\{\Psi_n^{\mathrm{A}};\mathrm{X}\}}, \\ v_2^{\mathrm{Y}} &= \frac{\sqrt{2}}{a_4^{-}} \frac{\langle \sin(2\phi)\sin(2\Psi_n^{\mathrm{A}})\rangle}{\mathrm{Res}\{\Psi_n^{\mathrm{A}};\mathrm{Y}\}}, \end{aligned} \tag{20}$$

where ϕ denotes the azimuthal angle of hadrons measured in the central arms and $a_4^{\pm} = 1 \pm \langle\cos(4\phi)\rangle$ are the acceptance correction factors of the measured v_2 in the central arms. The coefficient $a_4^{\pm}$ should be unity in the case of perfect azimuthal acceptance. $\mathrm{Res}\{\Psi_n^{\mathrm{A}};\mathrm{X}\}$ and $\mathrm{Res}\{\Psi_n^{\mathrm{A}};\mathrm{Y}\}$ denote the event-plane resolution for v_2^{X} and v_2^{Y}, respectively, and are expressed as

$$\begin{aligned} \mathrm{Res}\{\Psi_l^{\mathrm{A}};\mathrm{X}\} &= \sqrt{\langle \cos(2\Psi_l^{\mathrm{A}})\cos(2\Psi_m^{\mathrm{B}})\rangle} \\ &\quad\times\sqrt{\frac{\langle \cos(2\Psi_n^{\mathrm{C}})\cos(2\Psi_l^{\mathrm{A}})\rangle}{\langle \cos(2\Psi_m^{\mathrm{B}})\cos(2\Psi_n^{\mathrm{C}})\rangle}}, \\ \mathrm{Res}\{\Psi_l^{\mathrm{A}};\mathrm{Y}\} &= \sqrt{\langle \sin(2\Psi_l^{\mathrm{A}})\sin(2\Psi_m^{\mathrm{B}})\rangle} \\ &\quad\times\sqrt{\frac{\langle \sin(2\Psi_n^{\mathrm{C}})\sin(2\Psi_l^{\mathrm{A}})\rangle}{\langle \sin(2\Psi_m^{\mathrm{B}})\sin(2\Psi_n^{\mathrm{C}})\rangle}}, \end{aligned} \tag{21}$$

where l, m, n are the harmonics of event planes for subevents A, B, and C, respectively. Another acceptance effect from the difference between $\mathrm{Res}\{\Psi_n^{\mathrm{A}};\mathrm{X}\}$ and $\mathrm{Res}\{\Psi_n^{\mathrm{A}};\mathrm{Y}\}$ is discussed below.

Figure 13 shows the acceptance correction factor $a_4^{\pm}$ as a function of p_T in the central arms for centrality 0–60%. The p_T dependence is parametrized by

$$a_4^{\pm}(p_T) = 1 \mp \left(p_0 e^{-p_1 p_T} + \frac{p_2}{1 + e^{(p_T - p_3)/p_4}} + p_5 \right), \tag{22}$$

where $p_n (n = 0, 1, \ldots, 5)$ are free parameters. From the fit, we get $p_0 = 0.131$, $p_1 = 1.203$, $p_2 = 0.029$, $p_3 = 0.640$, $p_4 = 0.096$, and $p_5 = -0.097$. There is no centrality dependence of the acceptance corrections in the measured centrality range, and these same correction factors are applied for all centrality bins.

Figure 14 shows the raw $v_2\{\mathrm{BBC}\}$ as a function of p_T in the 20–60% centrality bin. v_2^{Y} is systematically higher than v_2^{X} for $p_T > 1$ GeV/c as shown in Fig. 14(a). Figure 14(b) shows that v_2^{X} and v_2^{Y} agree with each other after dividing v_2^{obs} by $a_4^{\pm}$, the remaining difference between them being accounted

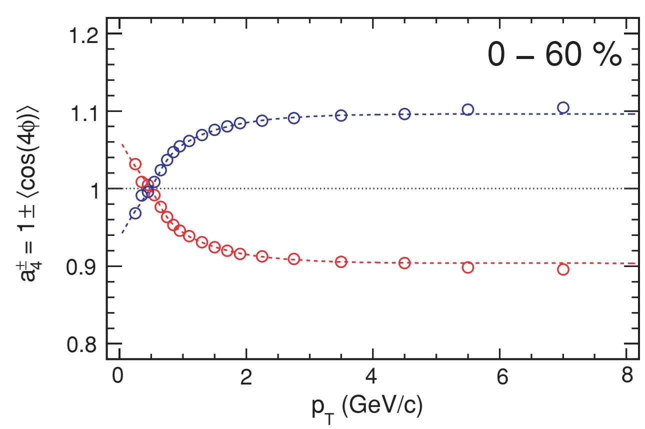

FIG. 13. (Color online) Acceptance correction factors $a_4^{\pm}$ in the central arms as a function of p_T for centrality 0–60%. Correction factors become unity for a perfect azimuthal acceptance. Statistical errors are smaller than the symbols.

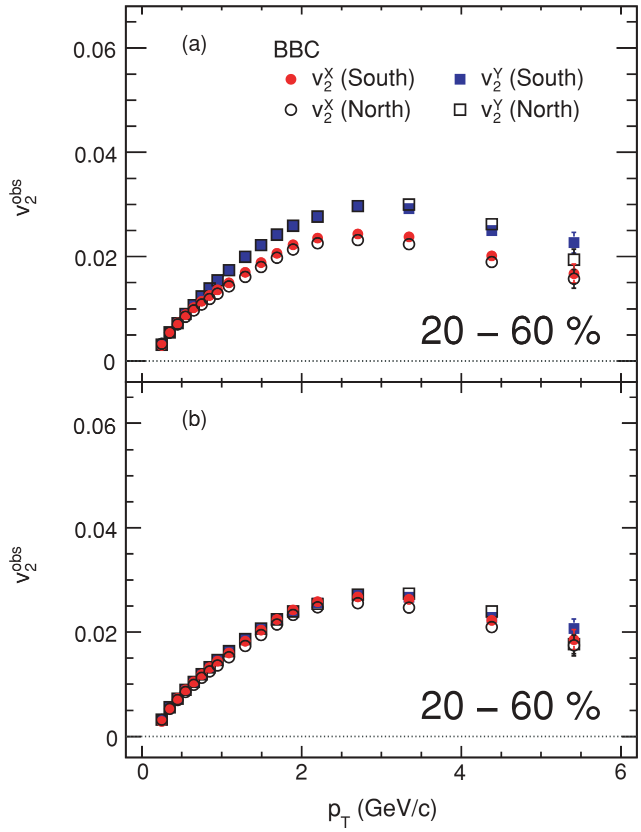

FIG. 14. (Color online) (a) Raw $v_2\{\text{BBC}\}$ without the acceptance correction as a function of p_T in centrality 20–60% for v_2^X and v_2^Y with the South and North BBC event planes. (b) Same comparison, but with the acceptance correction.

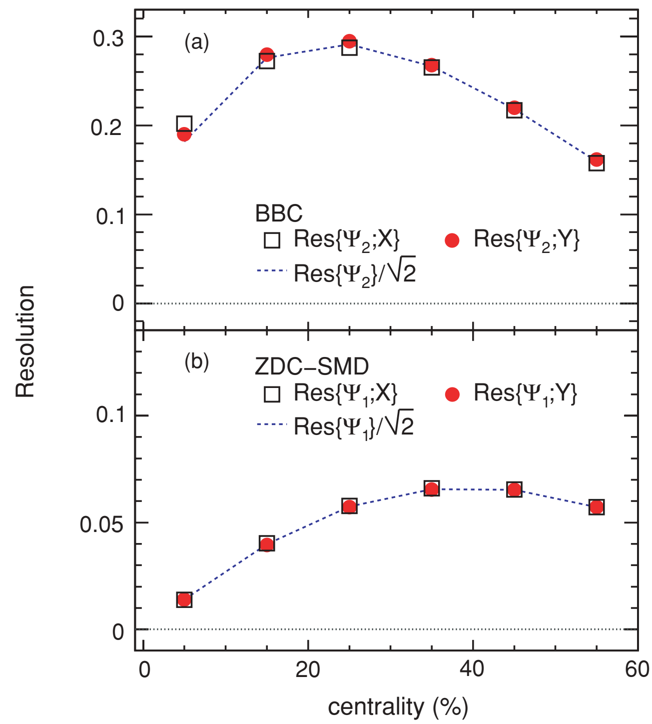

FIG. 15. (Color online) Comparison of $\text{Res}\{\Psi_n; \text{X}\}$ and $\text{Res}\{\Psi_n; \text{Y}\}$ with $\text{Res}\{\Psi_n\}$ for the (a) BBC event plane ($n = 2$) and (b) ZDC-SMD event plane ($n = 1$) as a function of centrality. The resolutions are calculated by using Eq. (21) with the ZDC-SMD, BBC, and CNT event planes. $\text{Res}\{\Psi_n\}$ is divided by $\sqrt{2}$ in order to compare $\text{Res}\{\Psi_n; \text{X}\}$ and $\text{Res}\{\Psi_n; \text{Y}\}$. Only statistical errors are shown and are smaller than symbols.

for as a systematic error. For the ZDC-SMD event plane, we observed a similar trend for v_2^X and v_2^Y.

A possible nonuniform acceptance of the BBC and ZDC-SMD could lead to the difference between $\text{Res}\{\Psi_n; \text{X}\}$ and $\text{Res}\{\Psi_n; \text{Y}\}$. If the azimuthal coverage of both detectors is perfect, $\text{Res}\{\Psi_n; \text{X}\}$ and $\text{Res}\{\Psi_n; \text{Y}\}$ should be identical. Therefore, the effect of the acceptance of the detector on the event-plane resolution can be assessed by comparing $\text{Res}\{\Psi_n; \text{X}\}$ and $\text{Res}\{\Psi_n; \text{Y}\}$.

Figure 15 shows $\text{Res}\{\Psi_n; \text{X}\}$ and $\text{Res}\{\Psi_n; \text{Y}\}$ of the BBC and ZDC-SMD as a function of centrality. The resolutions are calculated by using Eq. (21) with the ZDC-SMD, BBC, and CNT event planes. $\text{Res}\{\Psi_n; \text{X}\}$ was comparable to $\text{Res}\{\Psi_n; \text{Y}\}$ for both the BBC and ZDC-SMD event planes. They also agreed, within statistical errors, with the expected resolution, namely, the full-event resolution scaled by $1/\sqrt{2}$. We also evaluated $\text{Res}\{\Psi_n; \text{X}\}$ and $\text{Res}\{\Psi_n; \text{Y}\}$ of BBC and ZDC-SMD for the two-subevent method. $\text{Res}\{\Psi_2^{\text{BBC}}; \text{X}\}$ was consistent with $\text{Res}\{\Psi_2^{\text{BBC}}; \text{Y}\}$. However, for the ZDC-SMD event plane, $\text{Res}\{\Psi_1^{\text{ZDC-SMD}}; \text{Y}\}$ ($\text{Res}\{\Psi_1^{\text{ZDC-SMD}}; \text{X}\}$) was systematically higher (lower) by about 30% than the expected resolution when the resolutions were calculated with $k = 1$ in Eq. (8). The difference between $\text{Res}\{\Psi_1^{\text{ZDC-SMD}}; \text{X}\}$ and $\text{Res}\{\Psi_1^{\text{ZDC-SMD}}; \text{Y}\}$ for the two-subevent method is attributed to the nonuniform acceptance between horizontal (x) and vertical (y) directions of the ZDC-SMD. Those resolutions of the ZDC-SMD were consistent with each other using $k = 2$. For $k = 2$, the nonuniform acceptance in the azimuthal directions cancels out, since $\text{Res}\{\Psi_1^{\text{ZDC-SMD}}; \text{X, Y}\}$ contains both $\langle\cos(\Psi)\rangle$ and $\langle\sin(\Psi)\rangle$ terms. Thus, $\text{Res}\{\Psi_1^{\text{ZDC-SMD}}; \text{X, Y}\}$ should be the same and consistent with that from the expected resolution.

The comparison of v_2^X and v_2^Y with v_2 with respect to the BBC and ZDC-SMD event planes is shown in Fig. 16. The maximum difference of v_2^X and v_2^Y relative to $v_2\{\text{BBC}\}$ is about 2% for the centrality range 20–60% and is independent of centrality. Systematic uncertainties are evaluated by scaling the maximum difference by $2/\sqrt{12}$. The same comparison is also made for $v_2\{\text{ZDC-SMD}\}$ as shown in the bottom panel in Fig. 16. The systematic errors range from 1–25% and strongly depend on the centrality, as well as on the corrections by the different event-plane resolutions. v_2^X and v_2^Y are ~10–25% different from $v_2\{\text{ZDC-SMD}\}$ in the 0–20% centrality bin because of the very low resolution. This systematic uncertainty is denoted as "Acceptance effect on event planes" in Table III.

B. Cumulant method

The potential sources of systematic errors on the cumulant measurements are detailed below.

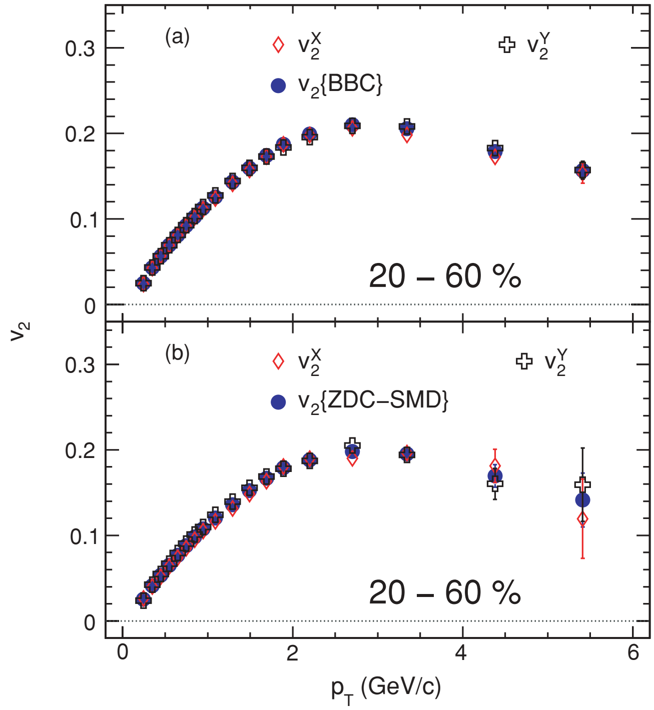

FIG. 16. (Color online) Comparison of v_2^X and v_2^Y with the total v_2 for the (a) BBC and (b) ZDC-SMD event planes as a function of p_T for the centrality bin 20–60%. Res$\{\Psi_n; X\}$ and Res$\{\Psi_n; Y\}$ are calculated by the combination of the ZDC-SMD, BBC, and CNT event planes. Acceptance corrections are included into v_2^X and v_2^Y. Error bars denote statistical errors.

1. Fixed multiplicity cut

Following Ref. [44], a fixed multiplicity is used to reconstruct the integrated flow to avoid introducing additional errors arising from a fluctuating multiplicity. In our analysis, the systematic errors were estimated by varying the fixed multiplicity cut used for the reconstruction of the integrated flow and studying its effect on the differential flow values.

Figure 17(a) shows the variation of v_2 with p_T for integral multiplicity cuts equal to 60%, 70%, and 80% of the mean multiplicity for the centrality bin 10–20%, which corresponds to 17, 20, and 22 particles, respectively. The ratio of the differential v_2 values, shown in Fig. 17(b), is used to estimate the systematic error on our measurements, which is ∼5%.

2. p_T range for integrated flow

To assess the influence of the p_T range used to estimate the integrated flow on the differential flow, we chose different p_T ranges over which the integral particles were selected. Differential v_2 results were obtained for three p_T ranges: 0.25–2.0, 0.25–1.5, and 0.3–1.5 GeV/c. The systematic error from this source is estimated to be 3–8% depending on centrality and p_T.

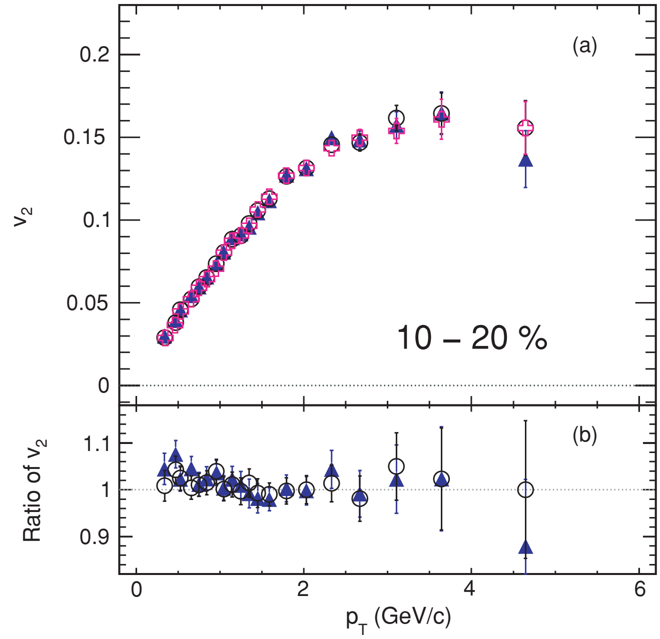

FIG. 17. (Color online) (a) $v_2\{2\}$ as a function of p_T for centrality 10–20% in Au + Au collisions at $\sqrt{s_{NN}} = 200$ GeV for different fixed multiplicity cuts, corresponding to 60% (filled triangles), 70% (open circles), and 80% (open crosses) of the mean multiplicity. (b) Ratio of $v_2(p_T)$ for the two lowest multiplicity cuts to $v_2(p_T)$ for 80% of the mean multiplicity.

3. Background contribution

The procedures followed for studying the background contribution to $v_2\{2\}$ were the same as for the event-plane method. After background subtraction, the systematic error is calculated by determining the difference between the v_2 obtained from using 2σ and 3σ association cuts. We determined that the overall systematic error due to these differences is 6–10% depending on p_T and centrality.

V. RESULTS

A. p_T dependence of v_2

The p_T dependence of v_2 has been instrumental in revealing the hydrodynamic properties of the matter formed at RHIC [19,21]. In this context, it is important to compare the p_T dependence of v_2 from different methods to establish the robustness of our v_2 measurements. This comparison is displayed in Fig. 18, which shows the differential charged hadron v_2 as a function of p_T from the event-plane and cumulant methods for different centrality bins in the range 0–60% in Au + Au at $\sqrt{s_{NN}} = 200$ GeV. $v_2\{2\}$ increases up to $p_T \approx 3$ GeV/c and saturates at 0.1–0.25, depending on centrality, for higher p_T. On the other hand, v_2\{BBC\} and v_2\{ZDC-SMD\} reach their maximum value at $p_T \approx 3$ GeV/c, and decrease for higher p_T.

The differences between v_2\{BBC\} and v_2\{ZDC-SMD\} are independent of p_T within systematic errors in the measured centrality range. v_2\{ZDC-SMD\} is consistent with v_2\{BBC\} within systematic errors in the 0–40% centrality range,

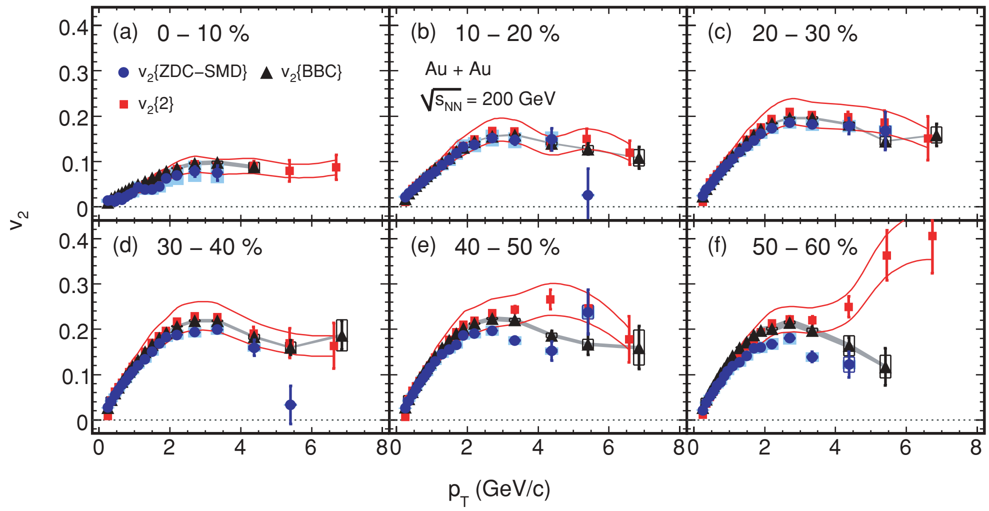

FIG. 18. (Color online) Charged hadron $v_2(p_T)$ in Au + Au collisions at $\sqrt{s_{NN}} = 200$ GeV from the two-particle cumulant method (filled squares), the BBC event plane (filled triangles), and the ZDC-SMD event plane (filled circles) for the indicated centralities. Error bars denote statistical errors. The type B systematic uncertainties are represented by the open boxes for the $v_2\{\mathrm{BBC}\}$ and $v_2\{\mathrm{ZDC\text{-}SMD}\}$, and by the solid lines for the $v_2\{2\}$. The gray bands and blue boxes represent the type C systematic uncertainties on the $v_2\{\mathrm{BBC}\}$ and $v_2\{\mathrm{ZDC\text{-}SMD}\}$, respectively.

but it is ∼10–20% smaller than $v_2\{\mathrm{BBC}\}$ in the 40–60% centrality range. These results could indicate that the influence of nonflow effects on $v_2\{\mathrm{BBC}\}$ is small and within the systematic errors, because nonflow effects are not expected to influence $v_2\{\mathrm{ZDC\text{-}SMD}\}$. The difference between $v_2\{\mathrm{BBC}\}$ and $v_2\{\mathrm{ZDC\text{-}SMD}\}$ in peripheral collisions could be attributed to nonflow contributions that might be proportionally larger in more peripheral collisions.

The cumulant and event-plane v_2 agree well within systematic uncertainties in the centrality range 0–40%. In more peripheral collisions, there may be some differences developing above $p_T \simeq 4$ GeV/c. Correlations between particles from jets affect the cumulant results, but have less influence on $v_2\{\mathrm{BBC}\}$, as explained in Ref. [29], where it was shown that the smaller the rapidity gap between the leading particle from a jet and the event plane, the greater the v_2 of the leading particle of the jet.

To illustrate more clearly the differences between the different methods, Fig. 19 shows the ratio of $v_2\{\mathrm{ZDC\text{-}SMD}\}$ and $v_2\{2\}$ to $v_2\{\mathrm{BBC}\}$. The results from the three methods are comparable in magnitude within systematic errors, except for the central and peripheral bins where the largest deviations occur. In addition, $v_2\{2\}$ and $v_2\{\mathrm{ZDC\text{-}SMD}\}$ show different behaviors at $p_T > 3$ GeV/c, with $v_2\{2\}$ being larger, and $v_2\{\mathrm{ZDC\text{-}SMD}\}$, smaller than $v_2\{\mathrm{BBC}\}$.

B. Centrality dependence of v_2

Figure 20 shows the N_{part} dependence of v_2 from different methods for charged hadrons in the range $1.0 < p_T <$

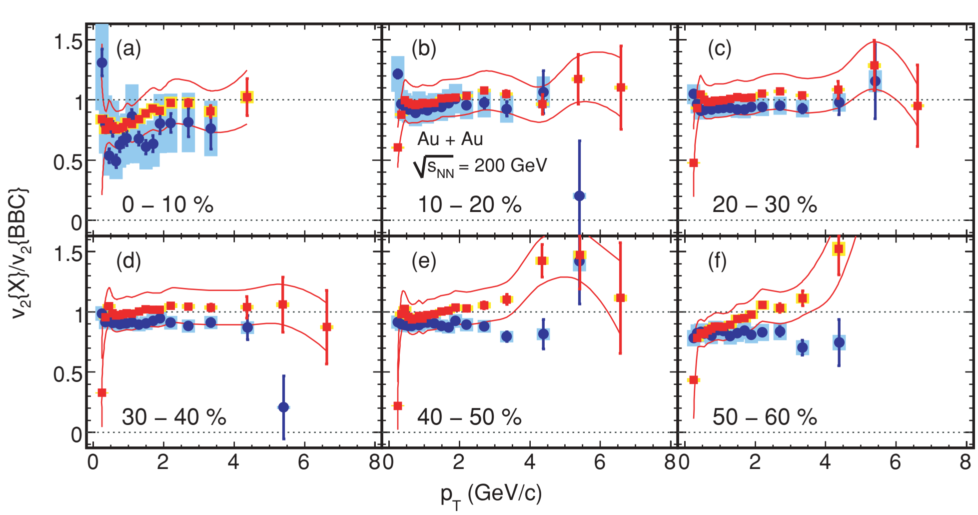

FIG. 19. (Color online) Ratio of v_2 to $v_2\{\mathrm{BBC}\}$ as a function of p_T for six centrality bins over the range 0–60% in Au + Au collisions at $\sqrt{s_{NN}} = 200$ GeV. Data symbols are the same as in the Fig. 18. Error bars denote statistical errors. The solid red lines represent the type B systematic errors on the $v_2\{2\}$. The blue and yellow bands represent type C systematic uncrtainties on $v_2\{\mathrm{ZDC\text{-}SMD}\}$ and $v_2\{2\}$.

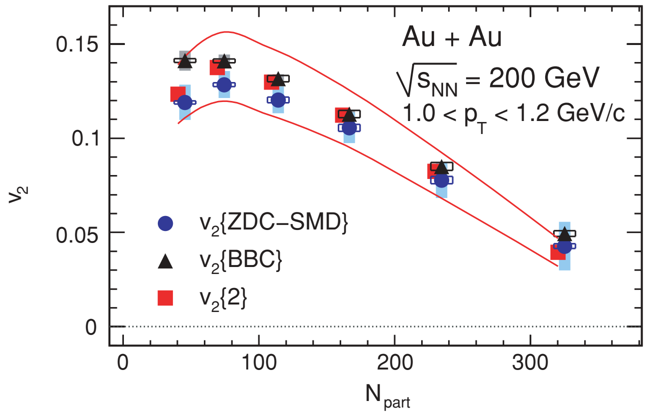

FIG. 20. (Color online) Comparison of charged hadron v_2 at $1 < p_T < 1.2$ GeV/c as a function of $N_{\rm part}$ for v_2\{BBC\}, v_2\{ZDC-SMD\}, and v_2\{2\} in Au + Au at $\sqrt{s_{NN}} = 200$ GeV. The error bars represent statistical errors. The open boxes represent type B systematic uncertainties on v_2\{BBC\} and v_2\{ZDC-SMD\}. Type B systematic uncertainties on v_2\{2\} are represented by solid red lines. The gray and blue bands represent type C systematic errors on v_2\{BBC\} and v_2\{ZDC-SMD\}, respectively. v_2\{2\} values are shifted in the x axis to improve the plot.

1.2 GeV/c. v_2 is observed to increase with decreasing $N_{\rm part}$ and then decrease slightly for $N_{\rm part} \lesssim 75$. Note that v_2 values obtained with the different methods agree well within systematic errors for all centralities. This is p_T dependent, as shown in Fig. 18.

C. Pseudorapidity dependence of v_2

Figure 21 compares the pseudorapidity dependence of the v_2 of charged hadrons within the η range (± 0.35) of the PHENIX central arms for different p_T selections. It can be observed that v_2 is constant over the η coverage of the PHENIX detector, and the constancy does not depend on p_T. This is not the case when the v_2 is measured far from midrapidity, where the PHOBOS and STAR Collaborations observe a drop in v_2 for $|\eta| > 1.0$ [49,50].

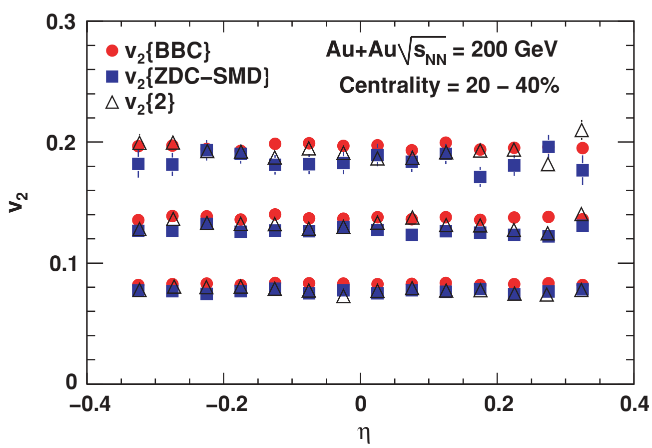

FIG. 21. (Color online) Anisotropy parameter v_2 as a function of pseudorapidity within the PHENIX central arms using event planes from the BBC and ZDC-SMD, and from the two-particle cumulant method for centrality 20–40%. The results are shown for three p_T bins, which are from top to bottom: 2.0–3.0, 1.2–1.4 and 0.6–0.8 GeV/c. Only statistical errors are shown.

VI. DISCUSSION

A. Effect of CNT event-plane resolution

Figure 22 shows the comparison of v_2\{ZDC-SMD\} and v_2\{BBC\} as a function of p_T corrected either by the resolution from South-North correlations from the same detectors or by the resolution from ZDC-SMD-CNT correlations in the 20–60% centrality bin. Figures 22(a) and 22(b) compare the v_2 obtained by using two different corrections from the South-North and ZDC-BBC-CNT subevents for the BBC and ZDC-SMD event planes. The v_2 from the South-North subevent is consistent with that from the ZDC-BBC-CNT subevent, within systematic uncertainties. The small difference between South-North and ZDC-BBC-CNT subevents is attributed to the difference between the event-plane resolution, as shown in Fig. 4. Figures 22(c) and 22(d) compare v_2\{ZDC-SMD\} with v_2\{BBC\} for the South-North and ZDC-BBC-CNT subevents. The data points in Figs. 22(c) and 22(d) are the same as in Figs. 22(a) and 22(b). Figure 22(c) shows that v_2\{ZDC-SMD\} is about 10% smaller than v_2\{BBC\} for the South-North subevent. The ratio of v_2\{ZDC-SMD\} to v_2\{BBC\} is found to be independent of p_T except for $6 < p_T < 8$ GeV/c. If jets are the dominant source of nonflow, one expects its contribution to v_2 to become larger at higher p_T. The constant ratio suggests that the nonflow contribution from jets is small, and v_2 fluctuations may affect v_2\{BBC\} below $p_T \approx 6$ GeV/c, since the effect of fluctuations is expected to be independent of p_T. v_2\{ZDC-SMD\} agrees with v_2\{BBC\} within systematic uncertainties for the ZDC-BBC-CNT subevent, as shown in Fig. 22(d). The event-plane resolution from the ZDC-BBC-CNT subevents includes the effect of nonflow contributions and v_2 fluctuations, since the CNT and BBC event planes are sensitive to both effects, though nonflow effects especially from jets could be negligible in the BBC event plane, as discussed earlier. The consistency between v_2 from the ZDC-SMD and BBC event planes may suggest that v_2\{ZDC-SMD\} becomes sensitive to v_2 fluctuations when the BBC and CNT event planes are included in the estimation of resolution.

B. Comparison with other experiments

It is instructive to compare measurements made by different experiments at RHIC. Figure 23 shows a comparison of the p_T dependence of charged hadron v_2 in the 20–60% centrality range between PHENIX and STAR experiments [51]. The relative systematic errors on the STAR v_2\{2\} and v_2\{4\} measurements range up to 10% for $p_T < 1$ GeV/c, with the lowest p_T bin having the largest error ∼10%, while they are of the order of 1% above 1 GeV/c [51]. The v_2\{2\} from PHENIX is lower than that from STAR, but they are comparable within

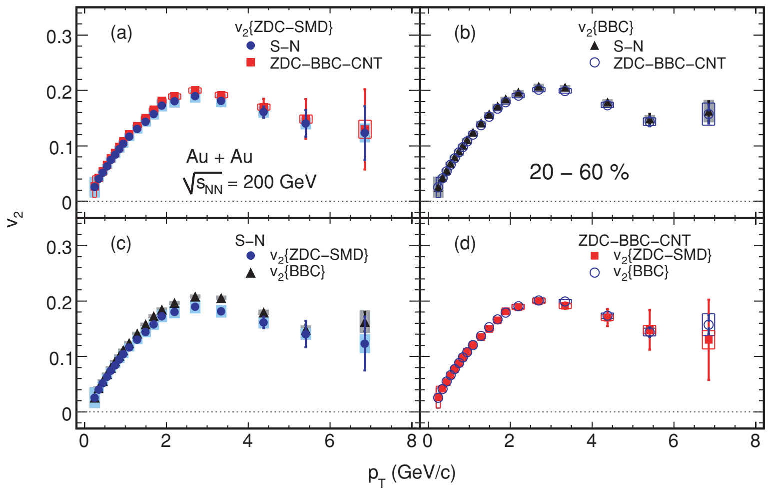

FIG. 22. (Color online) (a) Comparison of the $v_2\{\text{ZDC-SMD}\}$ obtained from the S-N and ZDC-BBC-CNT subevents as a function of p_T in the 20–60% centrality range. (b) Same comparison as (a), but for the $v_2\{\text{BBC}\}$. (c) Comparison of v_2 between BBC and ZDC-SMD event planes from the S-N subevent as a function of p_T in centrality 20–60%. (d) Same comparison as (c), but from the ZDC-BBC-CNT subevent. Error bars denote statistical errors. Open boxes and shaded bands describe the quadratic sum of type B and C systematic uncertainties from the S-N and ZDC-BBC-CNT subevents, respectively.

systematic uncertainties, as shown in Fig. 23(a). Figure 23(b) compares $v_2\{\text{BBC}\}$ and $v_2\{\text{ZDC-SMD}\}$ with $v_2\{4\}$, obtained from four-particle cumulants, as measured in STAR. For $p_T > 2$ GeV/c, the STAR $v_2\{4\}$ is systematically smaller than the PHENIX event-plane v_2, while $v_2\{\text{ZDC-SMD}\}$ is lower than $v_2\{\text{BBC}\}$. However, the three sets of measurements are consistent within systematic errors. The order of v_2, that is, $v_2\{\text{BBC}\} > v_2\{\text{ZDC-SMD}\} > v_2\{4\}$, could be explained by the effect of flow fluctuations [33,52] if other nonflow contributions are small.

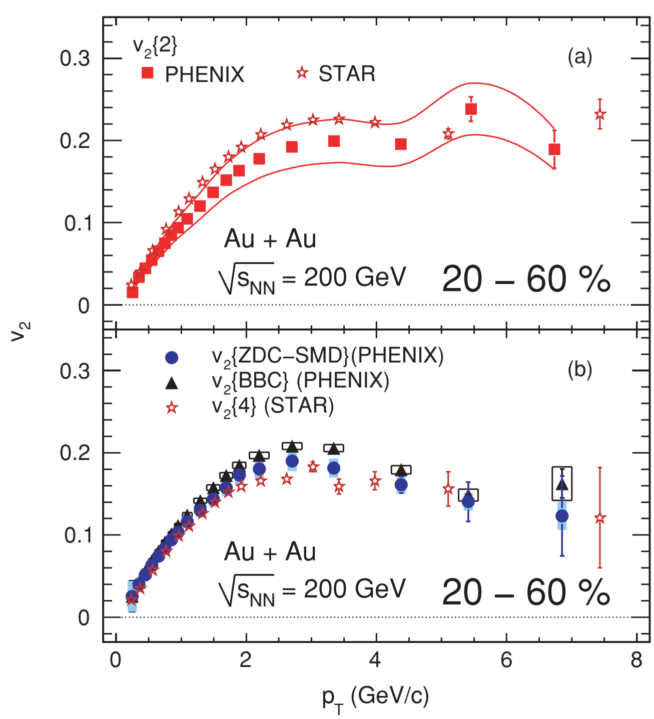

FIG. 23. (Color online) (a) Comparison of charged hadron $v_2\{2\}$ between PHENIX and STAR experiments as a function of p_T in centrality 20–60%. Solid lines represent the quadratic sum of type B and C systematic errors on the PHENIX $v_2\{2\}$. (b) Comparison of charged hadron v_2 from four-particle cumulant $v_2\{4\}$ at STAR with the PHENIX $v_2\{\text{BBC}\}$ and $v_2\{\text{ZDC-SMD}\}$ as a function of p_T in centrality 20–60%. Open boxes and shaded bands represent the quadratic sum of type B and C systematic errors on the $v_2\{\text{BBC}\}$ and $v_2\{\text{ZDC-SMD}\}$, respectively. STAR results are taken from Ref. [51]. Systematic errors on the STAR v_2 are not plotted, see text for more details.

Figure 24 compares our charged hadron v_2 from the BBC and ZDC-SMD event planes to v_2 from a modified event-plane method [49], labeled $v_2\{\text{EP}_2\}$, from the STAR experiment for three centrality bins in the range 10–40%. Particles within $|\Delta\eta| < 0.5$ around the highest p_T particle were excluded for the determination of the modified event plane in order to reduce some of the nonflow effects at high p_T. We find that $v_2\{\text{BBC}\}$ agrees well with $v_2\{\text{EP}_2\}$ over the measured p_T range, whereas $v_2\{\text{ZDC-SMD}\}$ is generally slightly smaller than $v_2\{\text{EP}_2\}$.

VII. SUMMARY

In summary, we have presented PHENIX elliptic flow measurements for unidentified charged hadrons from the event plane and the two-particle cumulant methods as a function of p_T and centrality at midrapidity ($|\eta| < 0.35$) in Au + Au collisions at $\sqrt{s_{NN}} = 200$ GeV. The first-harmonic ZDC-SMD event plane is used to measure v_2 and is compared with v_2 from the second-harmonic BBC event plane in order to understand the possible nonflow contributions as well as the effect of v_2 fluctuations on $v_2\{\text{BBC}\}$.

The comparison between v_2 from two-particle cumulant and event-plane methods shows that they agree within systematic errors. However, nonflow effects from jet correlations begin to contribute to the two-particle cumulant v_2, especially for peripheral collisions and at high p_T.

In contrast, nonflow effects on $v_2\{\text{BBC}\}$ are very small. The measured $v_2\{\text{BBC}\}$ values decrease by about 3% when the central arm event plane is included in the estimate of the BBC reaction plane resolution. This could be due to a

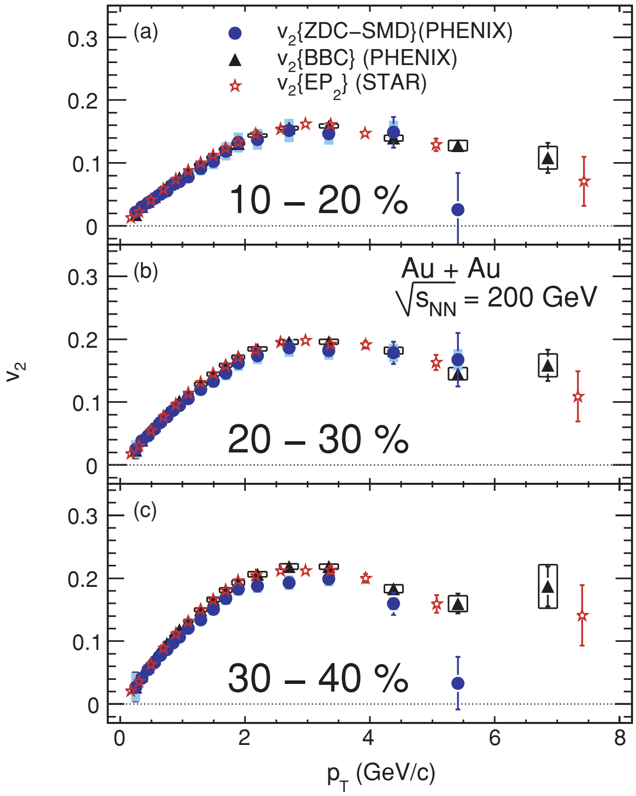

FIG. 24. (Color online) Comparison of the PHENIX $v_2\{\text{BBC}\}$ and $v_2\{\text{ZDC-SMD}\}$ with the STAR v_2 from the modified event-plane method for charged hadrons [49] as a function of p_T in three centralities. Open boxes and shaded bands represent the quadratic sum of type B and C systematic errors on $v_2\{\text{BBC}\}$ and $v_2\{\text{ZDC-SMD}\}$, respectively.

partial compensation of the nonflow effects on the measured v_2, though the results of $v_2\{\text{BBC}\}$ with and without the CNT event-plane resolution are consistent within systematic errors. The strongest evidence that nonflow effects on $v_2\{\text{BBC}\}$ are small comes from the observation that $v_2\{\text{ZDC-SMD}\}$ is comparable to $v_2\{\text{BBC}\}$ within systematic uncertainties in the 0–40% centrality range, and is only ∼5–10% smaller than $v_2\{\text{BBC}\}$ for the 40–60% centrality bin. The magnitude of this difference could indicate the level at which nonflow effects such as jets or the ridge could impact the measured flow. However, the PHOBOS Collaboration has observed the ridge to be strongest in central collisions [31] where we observe that $v_2\{\text{ZDC-SMD}\}$ is comparable with $v_2\{\text{BBC}\}$. For collisions that are more peripheral than 40% centrality, PHOBOS observes no ridge [31], so it is unlikely that our observation that $v_2\{\text{ZDC-SMD}\}$ is ∼5–10% smaller than $v_2\{\text{BBC}\}$ for the 40–60% centrality bin is caused by the ridge. Moreover, the difference between $v_2\{\text{ZDC-SMD}\}$ and $v_2\{\text{BBC}\}$ is independent of p_T in the measured centrality range.

Because of the large pseudorapidity gap between the event plane and the particles detected in the central arms spectrometer, and the first-harmonic event plane from directed flow by spectator neutrons, $v_2\{\text{ZDC-SMD}\}$ is considered to provide an unbiased measure of the elliptic flow. Within systematic uncertainties, the measured $v_2\{\text{ZDC-SMD}\}$ from PHENIX is consistent with v_2 from the four-particle cumulant method measured by the STAR experiment in the 20–60% centrality bin, and it is also consistent with the STAR v_2 from a modified event-plane method in 10–40% centrality bins. These comparisons (1) further demonstrate the validity of the $v_2\{\text{ZDC-SMD}\}$, because both STAR results aim to minimize the nonflow effects, (2) reinforce the robustness of the BBC event-plane method at RHIC, and (3) confirm previous studies of the influence of jets on the measured v_2 for different rapidity gaps. Hence, $v_2\{\text{BBC}\}$ can be used to infer constraints on the hydrodynamic behavior of heavy-ion collisions at RHIC.

ACKNOWLEDGMENTS

We thank the staff of the Collider-Accelerator and Physics Departments at Brookhaven National Laboratory and the staff of the other PHENIX participating institutions for their vital contributions. We acknowledge support from the Office of Nuclear Physics in the Office of Science of the US Department of Energy, the National Science Foundation, Abilene Christian University Research Council, Research Foundation of SUNY, and Dean of the College of Arts and Sciences, Vanderbilt University (USA), Ministry of Education, Culture, Sports, Science, and Technology and the Japan Society for the Promotion of Science (Japan), Conselho Nacional de Desenvolvimento Científico e Tecnológico and Fundação de Amparo à Pesquisa do Estado de São Paulo (Brazil), Natural Science Foundation of China (People's Republic of China), Centre National de la Recherche Scientifique, Commissariat à l'Énergie Atomique, and Institut National de Physique Nucléaire et de Physique des Particules (France), Ministry of Industry, Science and Tekhnologies, Bundesministerium für Bildung und Forschung, Deutscher Akademischer Austausch Dienst, and Alexander von Humboldt Stiftung (Germany), Hungarian National Science Fund, OTKA (Hungary), Department of Atomic Energy (India), Israel Science Foundation (Israel), Korea Research Foundation and Korea Science and Engineering Foundation (Korea), Ministry of Education and Science, Russia Academy of Sciences, Federal Agency of Atomic Energy (Russia), VR and the Wallenberg Foundation (Sweden), the US Civilian Research and Development Foundation for the Independent States of the Former Soviet Union, the US-Hungarian NSF-OTKA-MTA, and the US-Israel Binational Science Foundation.

APPENDIX: DATA TABLES OF v_2

Tables IV–X show numerical data in the same units as plotted in the figures: p_T (GeV/c), v_2, type A statistical error σ_{stat}, type B systematic error σ^B_{syst} and type C systematic error σ^C_{syst}.

TABLE IV. $v_2\{2\}$ as a function of p_T in centralities 0–10%, 10–20%, 20–30%, 30–40%, 40–50%, and 50–60%.

Centrality $v_1\{\}$	p_T (GeV/c)	v_2	σ_{stat}	σ_{syst}^{B}	σ_{syst}^{C}	Centrality $v_2\{\}$	p_T (GeV/c)	v_2	σ_{stat}	σ_{syst}^{B}	σ_{syst}^{C}
	0.247	0.00859	0.00014	0.00001	0.00000		0.250	0.00898	0.00021	0.00001	0.00000
	0.347	0.01406	0.00019	0.00004	0.00000		0.349	0.04323	0.00030	0.00026	0.00000
	0.450	0.01882	0.00023	0.00007	0.00000		0.448	0.06214	0.00036	0.00053	0.00000
	0.547	0.02140	0.00027	0.00009	0.00000		0.548	0.07193	0.00042	0.00071	0.00000
	0.649	0.02395	0.00031	0.00011	0.00000		0.648	0.08243	0.00048	0.00093	0.00000
	0.748	0.02718	0.00036	0.00014	0.00000		0.748	0.09401	0.00055	0.00121	0.00000
	0.847	0.03087	0.00041	0.00018	0.00000		0.848	0.10533	0.00063	0.00153	0.00000
	0.949	0.03605	0.00047	0.00024	0.00000		0.948	0.11678	0.00071	0.00187	0.00000
	1.090	0.03950	0.00041	0.00029	0.00000		1.092	0.12972	0.00063	0.00231	0.00000
0–10%	1.291	0.04734	0.00053	0.00042	0.00000	30–40%	1.291	0.15059	0.00081	0.00312	0.00000
$v_2\{2\}$	1.490	0.05633	0.00070	0.00059	0.00000	$v_2\{2\}$	1.489	0.16955	0.00107	0.00395	0.00000
	1.689	0.06542	0.00095	0.00080	0.00000		1.689	0.18422	0.00147	0.00467	0.00000
	1.890	0.07148	0.00128	0.00096	0.00000		1.891	0.19625	0.00198	0.00529	0.00000
	2.194	0.08352	0.00128	0.00130	0.00000		2.197	0.21718	0.00196	0.00648	0.00000
	2.698	0.09362	0.00249	0.00164	0.00000		2.702	0.22835	0.00369	0.00717	0.00000
	3.329	0.08866	0.00421	0.00147	0.00000		3.338	0.22623	0.00556	0.00704	0.00000
	4.365	0.08997	0.01134	0.00151	0.00000		4.360	0.19059	0.01496	0.00499	0.00000
	5.376	0.07933	0.02365	0.00118	0.00000		5.379	0.16931	0.03256	0.00394	0.00000
	6.695	0.08701	0.02720	0.00142	0.00000		6.628	0.16346	0.05010	0.00367	0.00000
	0.248	0.01089	0.00013	0.00002	0.00000		0.250	0.00625	0.00032	0.00001	0.00000
	0.348	0.02714	0.00018	0.00011	0.00000		0.349	0.04611	0.00044	0.00028	0.00000
	0.449	0.03914	0.00023	0.00023	0.00000		0.448	0.06387	0.00054	0.00054	0.00000
	0.547	0.04592	0.00027	0.00032	0.00000		0.548	0.07455	0.00062	0.00073	0.00000
	0.649	0.05281	0.00030	0.00042	0.00000		0.648	0.08575	0.00072	0.00097	0.00000
	0.748	0.05977	0.00035	0.00054	0.00000		0.748	0.09774	0.00082	0.00126	0.00000
	0.848	0.06637	0.00040	0.00066	0.00000		0.848	0.11126	0.00094	0.00163	0.00000
	0.948	0.07459	0.00045	0.00083	0.00000		0.948	0.11974	0.00108	0.00189	0.00000
	1.092	0.08249	0.00040	0.00102	0.00000		1.092	0.13745	0.00095	0.00249	0.00000
10–20%	1.291	0.09506	0.00051	0.00136	0.00000	40–50%	1.291	0.15672	0.00123	0.00324	0.00000
$v_2\{2\}$	1.490	0.10997	0.00067	0.00181	0.00000	$v_2\{2\}$	1.489	0.17633	0.00166	0.00410	0.00000
	1.689	0.12394	0.00090	0.00230	0.00000		1.689	0.19315	0.00229	0.00492	0.00000
	1.891	0.13378	0.00121	0.00268	0.00000		1.891	0.20965	0.00309	0.00580	0.00000
	2.196	0.14881	0.00121	0.00332	0.00000		2.199	0.21909	0.00304	0.00633	0.00000
	2.699	0.16781	0.00232	0.00422	0.00000		2.701	0.23572	0.00567	0.00733	0.00000
	3.328	0.16669	0.00382	0.00417	0.00000		3.344	0.24331	0.00808	0.00781	0.00000
	4.357	0.13468	0.01047	0.00272	0.00000		4.346	0.26575	0.02124	0.00932	0.00000
	5.371	0.14951	0.02244	0.00335	0.00000		5.414	0.24613	0.03288	0.00799	0.00000
	6.587	0.11931	0.02641	0.00214	0.00000		6.566	0.17786	0.05097	0.00417	0.00000
	0.249	0.01127	0.00015	0.00002	0.00000		0.251	0.01201	0.00052	0.00002	0.00000
	0.349	0.03713	0.00022	0.00019	0.00000		0.349	0.03575	0.00056	0.00016	0.00000
	0.448	0.05370	0.00028	0.00040	0.00000		0.448	0.05111	0.00063	0.00033	0.00000
	0.548	0.06252	0.00032	0.00054	0.00000		0.548	0.06256	0.00071	0.00050	0.00000
	0.648	0.07147	0.00036	0.00070	0.00000		0.648	0.07591	0.00080	0.00073	0.00000
	0.748	0.08144	0.00041	0.00091	0.00000		0.748	0.08903	0.00091	0.00101	0.00000
	0.848	0.09118	0.00047	0.00114	0.00000		0.848	0.09965	0.00103	0.00126	0.00000
	0.948	0.10071	0.00053	0.00139	0.00000		0.948	0.11124	0.00118	0.00157	0.00000
	1.092	0.11227	0.00047	0.00173	0.00000		1.091	0.12340	0.00103	0.00193	0.00000
20–30%	1.291	0.12982	0.00060	0.00232	0.00000	50–60%	1.290	0.14241	0.00133	0.00257	0.00000
$v_2\{2\}$	1.489	0.14786	0.00079	0.00301	0.00000	$v_2\{2\}$	1.489	0.16236	0.00178	0.00334	0.00000
	1.689	0.16113	0.00107	0.00357	0.00000		1.689	0.17737	0.00248	0.00399	0.00000
	1.891	0.17515	0.00145	0.00422	0.00000		1.890	0.19295	0.00337	0.00472	0.00000
	2.196	0.19364	0.00143	0.00515	0.00000		2.198	0.21282	0.00330	0.00575	0.00000
	2.699	0.20931	0.00271	0.00602	0.00000		2.700	0.22201	0.00623	0.00625	0.00000
	3.333	0.20299	0.00430	0.00567	0.00000		3.348	0.21980	0.00917	0.00613	0.00000
	4.356	0.19729	0.01175	0.00535	0.00000		4.373	0.24935	0.02292	0.00789	0.00000
	5.383	0.18635	0.02567	0.00477	0.00000		5.452	0.36285	0.05515	0.01671	0.00000
	6.611	0.15079	0.04839	0.00313	0.00000		6.734	0.40554	0.08167	0.02087	0.00000

TABLE V. $v_2\{2\}$ as a function of p_T in centrality 20–60%.

Centrality $v_2\{\}$	p_T (GeV/c)	v_2	σ_{stat}	$\sigma_{\mathrm{syst}}^{B}$	$\sigma_{\mathrm{syst}}^{C}$	p_T (GeV/c)	v_2	σ_{stat}	$\sigma_{\mathrm{syst}}^{B}$	$\sigma_{\mathrm{syst}}^{C}$
20–60% $v_2\{2\}$	0.251	0.00778	0.00011	0.00001	0.00000	1.489	0.14884	0.00058	0.00292	0.00000
	0.349	0.03793	0.00016	0.00019	0.00000	1.689	0.16226	0.00080	0.00347	0.00000
	0.448	0.05476	0.00020	0.00040	0.00000	1.890	0.17456	0.00108	0.00402	0.00000
	0.548	0.06374	0.00023	0.00054	0.00000	2.198	0.19027	0.00106	0.00478	0.00000
	0.648	0.07303	0.00026	0.00070	0.00000	2.700	0.20415	0.00201	0.00550	0.00000
	0.748	0.08283	0.00030	0.00091	0.00000	3.348	0.21363	0.00304	0.00602	0.00000
	0.848	0.09301	0.00034	0.00114	0.00000	4.373	0.19568	0.00653	0.00505	0.00000
	0.948	0.10247	0.00039	0.00139	0.00000	5.452	0.23823	0.01494	0.00749	0.00000
	1.091	0.11444	0.00034	0.00173	0.00000	6.734	0.18915	0.02297	0.00472	0.00000
	1.290	0.13201	0.00044	0.00230	0.00000					

TABLE VI. $v_2\{\mathrm{BBC}\}$ and $v_2\{\mathrm{ZDC\text{-}SMD}\}$ from S-N and ZDC-BBC-CNT subevents as a function of p_T in centrality 20–60%.

Centrality $v_2\{\}$	p_T (GeV/c)	S-N subevents				ZDC-BBC-CNT subevents			
		v_2	σ_{stat}	$\sigma_{\mathrm{syst}}^{B}$	$\sigma_{\mathrm{syst}}^{C}$	v_2	σ_{stat}	$\sigma_{\mathrm{syst}}^{B}$	$\sigma_{\mathrm{syst}}^{C}$
20–60% $v_2\{\mathrm{BBC}\}$	0.247	0.02569	0.00009	0.00049	0.00001	0.02486	0.00009	0.00045	0.00001
	0.348	0.04271	0.00009	0.00016	0.00003	0.04133	0.00010	0.00015	0.00003
	0.448	0.05587	0.00010	0.00014	0.00006	0.05407	0.00012	0.00013	0.00005
	0.548	0.06846	0.00011	0.00015	0.00009	0.06625	0.00013	0.00014	0.00008
	0.648	0.08009	0.00013	0.00015	0.00012	0.07751	0.00015	0.00014	0.00011
	0.748	0.09123	0.00014	0.00016	0.00015	0.08828	0.00017	0.00015	0.00014
	0.848	0.10124	0.00016	0.00019	0.00019	0.09798	0.00019	0.00018	0.00018
	0.948	0.11159	0.00018	0.00017	0.00023	0.10799	0.00021	0.00016	0.00021
	1.092	0.12439	0.00016	0.00018	0.00029	0.12038	0.00020	0.00017	0.00027
	1.292	0.14170	0.00020	0.00019	0.00037	0.13713	0.00025	0.00018	0.00035
	1.492	0.15770	0.00027	0.00027	0.00046	0.15261	0.00031	0.00025	0.00043
	1.692	0.17244	0.00037	0.00027	0.00055	0.16688	0.00040	0.00026	0.00051
	1.892	0.18481	0.00050	0.00030	0.00063	0.17885	0.00052	0.00028	0.00059
	2.200	0.19684	0.00049	0.00029	0.00071	0.19049	0.00052	0.00027	0.00067
	2.703	0.20803	0.00092	0.00025	0.00080	0.20132	0.00092	0.00023	0.00075
	3.343	0.20569	0.00141	0.00039	0.00078	0.19905	0.00138	0.00037	0.00073
	4.381	0.17942	0.00371	0.00066	0.00059	0.17363	0.00360	0.00062	0.00056
	5.410	0.14862	0.00877	0.00098	0.00041	0.14382	0.00849	0.00092	0.00038
	6.852	0.16262	0.01770	0.00328	0.00049	0.15738	0.01713	0.00308	0.00046
20–60% $v_2\{\mathrm{ZDC\text{-}SMD}\}$	0.247	0.02532	0.00025	0.00047	0.00004	0.02661	0.00035	0.00052	0.00002
	0.348	0.04002	0.00029	0.00014	0.00010	0.04188	0.00037	0.00015	0.00004
	0.448	0.05165	0.00032	0.00012	0.00017	0.05395	0.00041	0.00013	0.00007
	0.548	0.06296	0.00036	0.00013	0.00025	0.06567	0.00046	0.00014	0.00010
	0.648	0.07433	0.00041	0.00013	0.00035	0.07746	0.00051	0.00014	0.00014
	0.748	0.08377	0.00046	0.00013	0.00044	0.08730	0.00057	0.00015	0.00017
	0.848	0.09429	0.00052	0.00017	0.00056	0.09827	0.00065	0.00018	0.00022
	0.948	0.10365	0.00059	0.00015	0.00067	0.10808	0.00074	0.00016	0.00027
	1.092	0.11617	0.00053	0.00016	0.00085	0.12065	0.00063	0.00017	0.00033
	1.292	0.13006	0.00066	0.00016	0.00106	0.13535	0.00081	0.00018	0.00042
	1.492	0.14367	0.00086	0.00023	0.00129	0.14994	0.00109	0.00024	0.00052
	1.692	0.15763	0.00115	0.00023	0.00156	0.16504	0.00150	0.00025	0.00062
	1.892	0.17281	0.00151	0.00026	0.00187	0.18136	0.00203	0.00029	0.00075
	2.200	0.18031	0.00149	0.00024	0.00204	0.18912	0.00200	0.00026	0.00082
	2.703	0.18983	0.00263	0.00021	0.00226	0.19998	0.00375	0.00023	0.00092
	3.343	0.18147	0.00393	0.00030	0.00206	0.19147	0.00576	0.00034	0.00084
	4.381	0.16102	0.01018	0.00053	0.00162	0.17005	0.01517	0.00059	0.00066
	5.410	0.14043	0.02402	0.00088	0.00124	0.14833	0.03585	0.00098	0.00050
	6.852	0.12310	0.04849	0.00188	0.00095	0.13003	0.07240	0.00210	0.00039

TABLE VII. $v_2\{\mathrm{BBC}\}$ from S-N and ZDC-BBC-CNT subevents as a function of p_T in centrality 0–10%, 10–20%, and 20–30%.

Centrality $v_2\{\}$	p_T (GeV/c)	S-N subevents				ZDC-BBC-CNT subevents			
		v_2	σ_{stat}	σ^B_{syst}	σ^C_{syst}	v_2	σ_{stat}	σ^B_{syst}	σ^C_{syst}
	0.247	0.01025	0.00012	0.00008	0.00001	0.00966	0.00016	0.00007	0.00000
	0.348	0.01868	0.00014	0.00003	0.00002	0.01762	0.00025	0.00003	0.00002
	0.448	0.02300	0.00016	0.00005	0.00003	0.02169	0.00030	0.00005	0.00002
	0.548	0.02741	0.00018	0.00007	0.00004	0.02586	0.00035	0.00006	0.00003
	0.648	0.03174	0.00020	0.00007	0.00005	0.02993	0.00041	0.00006	0.00005
	0.748	0.03570	0.00023	0.00007	0.00006	0.03367	0.00046	0.00006	0.00006
	0.848	0.03990	0.00026	0.00007	0.00008	0.03763	0.00051	0.00006	0.00007
	0.948	0.04428	0.00029	0.00008	0.00010	0.04176	0.00057	0.00007	0.00009
	1.092	0.04941	0.00025	0.00008	0.00012	0.04660	0.00061	0.00007	0.00011
0–10%	1.292	0.05631	0.00032	0.00008	0.00016	0.05310	0.00070	0.00007	0.00014
$v_2\{\mathrm{BBC}\}$	1.492	0.06349	0.00042	0.00008	0.00020	0.05988	0.00082	0.00007	0.00018
	1.692	0.07065	0.00058	0.00012	0.00025	0.06663	0.00096	0.00010	0.00022
	1.892	0.07859	0.00078	0.00011	0.00031	0.07412	0.00115	0.00010	0.00028
	2.200	0.08557	0.00078	0.00009	0.00037	0.08070	0.00121	0.00008	0.00033
	2.703	0.09598	0.00151	0.00015	0.00046	0.09052	0.00179	0.00014	0.00041
	3.343	0.09806	0.00245	0.00031	0.00049	0.09249	0.00257	0.00028	0.00043
	4.381	0.08795	0.00699	0.00089	0.00039	0.08295	0.00667	0.00079	0.00035
	0.247	0.01804	0.00010	0.00008	0.00000	0.01754	0.00011	0.00007	0.00000
	0.348	0.03095	0.00011	0.00008	0.00001	0.03008	0.00015	0.00008	0.00001
	0.448	0.03927	0.00012	0.00012	0.00002	0.03816	0.00018	0.00011	0.00002
	0.548	0.04714	0.00014	0.00018	0.00003	0.04582	0.00020	0.00017	0.00003
	0.648	0.05480	0.00015	0.00016	0.00004	0.05326	0.00023	0.00015	0.00004
	0.748	0.06236	0.00017	0.00016	0.00006	0.06060	0.00026	0.00015	0.00005
	0.848	0.06895	0.00019	0.00016	0.00007	0.06701	0.00029	0.00015	0.00006
	0.948	0.07647	0.00022	0.00017	0.00008	0.07432	0.00033	0.00016	0.00008
	1.092	0.08498	0.00019	0.00018	0.00010	0.08259	0.00033	0.00017	0.00010
10–20%	1.292	0.09731	0.00024	0.00018	0.00014	0.09457	0.00040	0.00017	0.00013
$v_2\{\mathrm{BBC}\}$	1.492	0.10883	0.00032	0.00022	0.00017	0.10576	0.00047	0.00021	0.00016
	1.692	0.12204	0.00044	0.00021	0.00021	0.11860	0.00058	0.00020	0.00020
	1.892	0.13129	0.00059	0.00029	0.00025	0.12760	0.00072	0.00027	0.00023
	2.200	0.14375	0.00058	0.00021	0.00030	0.13970	0.00074	0.00020	0.00028
	2.703	0.15569	0.00112	0.00023	0.00035	0.15130	0.00120	0.00022	0.00033
	3.343	0.15885	0.00177	0.00033	0.00037	0.15437	0.00180	0.00031	0.00034
	4.381	0.13970	0.00491	0.00056	0.00028	0.13577	0.00480	0.00053	0.00027
	5.410	0.12763	0.01194	0.00101	0.00024	0.12403	0.01161	0.00095	0.00022
	6.852	0.10820	0.02401	0.00193	0.00017	0.10515	0.02334	0.00183	0.00016
	0.247	0.02367	0.00011	0.00032	0.00001	0.02303	0.00012	0.00030	0.00001
	0.348	0.03981	0.00012	0.00014	0.00002	0.03874	0.00015	0.00014	0.00002
	0.448	0.05138	0.00014	0.00016	0.00004	0.04999	0.00017	0.00015	0.00004
	0.548	0.06250	0.00015	0.00019	0.00006	0.06081	0.00020	0.00018	0.00005
	0.648	0.07276	0.00017	0.00020	0.00008	0.07080	0.00023	0.00019	0.00007
	0.748	0.08298	0.00019	0.00018	0.00010	0.08075	0.00026	0.00017	0.00010
	0.848	0.09184	0.00022	0.00020	0.00012	0.08937	0.00029	0.00019	0.00012
	0.948	0.10139	0.00024	0.00020	0.00015	0.09866	0.00032	0.00019	0.00014
	1.092	0.11279	0.00021	0.00022	0.00019	0.10976	0.00032	0.00021	0.00018
20–30%	1.292	0.12862	0.00027	0.00023	0.00024	0.12516	0.00038	0.00022	0.00023
$v_2\{\mathrm{BBC}\}$	1.492	0.14459	0.00036	0.00029	0.00031	0.14070	0.00046	0.00027	0.00029
	1.692	0.15864	0.00049	0.00030	0.00037	0.15437	0.00058	0.00029	0.00035
	1.892	0.17169	0.00066	0.00032	0.00043	0.16707	0.00074	0.00030	0.00041
	2.200	0.18437	0.00065	0.00032	0.00050	0.17941	0.00075	0.00030	0.00047
	2.703	0.19554	0.00123	0.00042	0.00056	0.19028	0.00127	0.00039	0.00053
	3.343	0.19585	0.00192	0.00048	0.00056	0.19058	0.00192	0.00046	0.00053
	4.381	0.18189	0.00521	0.00088	0.00049	0.17700	0.00509	0.00083	0.00046
	5.410	0.14502	0.01244	0.00138	0.00031	0.14112	0.01211	0.00131	0.00029
	6.852	0.15856	0.02490	0.00286	0.00037	0.15430	0.02423	0.00271	0.00035

TABLE VIII. v_2\{BBC\} from S-N and ZDC-BBC-CNT subevents as a function of p_T in centrality 30–40%, 40–50%, and 50–60%.

Centrality $v_2\{\}$	p_T (GeV/c)	S-N subevents				ZDC-BBC-CNT subevents			
		v_2	$\sigma_{\rm stat}$	$\sigma^B_{\rm syst}$	$\sigma^C_{\rm syst}$	v_2	$\sigma_{\rm stat}$	$\sigma^B_{\rm syst}$	$\sigma^C_{\rm syst}$
	0.247	0.02733	0.00015	0.00064	0.00001	0.02643	0.00016	0.00059	0.00001
	0.348	0.04523	0.00016	0.00017	0.00004	0.04375	0.00018	0.00016	0.00003
	0.448	0.05935	0.00018	0.00017	0.00006	0.05740	0.00021	0.00016	0.00006
	0.548	0.07263	0.00020	0.00016	0.00010	0.07024	0.00024	0.00015	0.00009
	0.648	0.08502	0.00023	0.00015	0.00013	0.08223	0.00028	0.00014	0.00012
	0.748	0.09651	0.00025	0.00020	0.00017	0.09334	0.00031	0.00018	0.00016
	0.848	0.10742	0.00029	0.00019	0.00021	0.10390	0.00035	0.00018	0.00020
	0.948	0.11793	0.00033	0.00018	0.00025	0.11406	0.00039	0.00017	0.00024
	1.092	0.13156	0.00028	0.00022	0.00032	0.12724	0.00038	0.00020	0.00030
30–40%	1.292	0.15004	0.00036	0.00019	0.00041	0.14512	0.00046	0.00018	0.00038
v_2\{BBC\}	1.492	0.16604	0.00048	0.00030	0.00050	0.16059	0.00057	0.00028	0.00047
	1.692	0.18107	0.00066	0.00029	0.00060	0.17513	0.00073	0.00027	0.00056
	1.892	0.19290	0.00089	0.00034	0.00068	0.18657	0.00094	0.00032	0.00063
	2.200	0.20640	0.00088	0.00035	0.00078	0.19962	0.00094	0.00032	0.00073
	2.703	0.21859	0.00164	0.00042	0.00087	0.21142	0.00164	0.00040	0.00081
	3.343	0.21843	0.00252	0.00037	0.00087	0.21127	0.00247	0.00034	0.00081
	4.381	0.18342	0.00662	0.00101	0.00061	0.17740	0.00641	0.00095	0.00057
	5.410	0.15970	0.01568	0.00197	0.00046	0.15446	0.01517	0.00184	0.00043
	6.852	0.18703	0.03171	0.00640	0.00064	0.18090	0.03067	0.00599	0.00060
	0.247	0.02840	0.00024	0.00071	0.00002	0.02735	0.00024	0.00066	0.00002
	0.348	0.04699	0.00025	0.00018	0.00005	0.04524	0.00027	0.00017	0.00005
	0.448	0.06236	0.00028	0.00015	0.00009	0.06005	0.00031	0.00014	0.00009
	0.548	0.07757	0.00031	0.00015	0.00014	0.07469	0.00035	0.00014	0.00013
	0.648	0.09141	0.00035	0.00015	0.00020	0.08802	0.00040	0.00014	0.00018
	0.748	0.10354	0.00039	0.00016	0.00025	0.09969	0.00045	0.00015	0.00024
	0.848	0.11530	0.00044	0.00019	0.00032	0.11102	0.00051	0.00017	0.00029
	0.948	0.12668	0.00050	0.00016	0.00038	0.12198	0.00057	0.00015	0.00035
	1.092	0.14106	0.00044	0.00015	0.00047	0.13583	0.00054	0.00014	0.00044
40–50%	1.292	0.15967	0.00056	0.00019	0.00061	0.15374	0.00066	0.00017	0.00056
v_2\{BBC\}	1.492	0.17584	0.00075	0.00025	0.00074	0.16932	0.00083	0.00023	0.00068
	1.692	0.19082	0.00104	0.00031	0.00087	0.18373	0.00110	0.00029	0.00080
	1.892	0.20216	0.00141	0.00031	0.00097	0.19466	0.00144	0.00029	0.00090
	2.200	0.21274	0.00138	0.00031	0.00108	0.20485	0.00142	0.00029	0.00100
	2.703	0.22348	0.00256	0.00039	0.00119	0.21518	0.00252	0.00036	0.00110
	3.343	0.22044	0.00387	0.00067	0.00116	0.21226	0.00376	0.00063	0.00107
	4.381	0.18665	0.00994	0.00094	0.00083	0.17973	0.00958	0.00087	0.00077
	5.410	0.16716	0.02325	0.00178	0.00067	0.16095	0.02239	0.00165	0.00062
	6.852	0.15951	0.04732	0.00616	0.00060	0.15359	0.04556	0.00571	0.00056
	0.247	0.02767	0.00043	0.00056	0.00003	0.02604	0.00042	0.00050	0.00003
	0.348	0.04569	0.00046	0.00019	0.00008	0.04300	0.00046	0.00017	0.00007
	0.448	0.06193	0.00050	0.00018	0.00014	0.05828	0.00052	0.00016	0.00013
	0.548	0.07654	0.00056	0.00014	0.00022	0.07203	0.00060	0.00013	0.00019
	0.648	0.08963	0.00064	0.00013	0.00030	0.08435	0.00068	0.00012	0.00027
	0.748	0.10358	0.00072	0.00014	0.00040	0.09747	0.00077	0.00012	0.00036
	0.848	0.11362	0.00082	0.00020	0.00048	0.10692	0.00087	0.00018	0.00043
	0.948	0.12637	0.00093	0.00011	0.00060	0.11892	0.00099	0.00010	0.00053
	1.092	0.14117	0.00082	0.00014	0.00075	0.13284	0.00091	0.00012	0.00066
50–60%	1.292	0.15953	0.00105	0.00020	0.00095	0.15013	0.00114	0.00017	0.00085
v_2\{BBC\}	1.492	0.17233	0.00141	0.00028	0.00111	0.16217	0.00146	0.00024	0.00099
	1.692	0.18714	0.00196	0.00029	0.00131	0.17611	0.00196	0.00026	0.00116
	1.892	0.19757	0.00266	0.00054	0.00146	0.18592	0.00260	0.00047	0.00130
	2.200	0.20146	0.00260	0.00054	0.00152	0.18959	0.00255	0.00048	0.00135
	2.703	0.21521	0.00480	0.00066	0.00174	0.20252	0.00458	0.00059	0.00154
	3.343	0.19757	0.00712	0.00083	0.00146	0.18593	0.00674	0.00074	0.00130
	4.381	0.16368	0.01791	0.00363	0.00100	0.15403	0.01686	0.00321	0.00089
	5.410	0.11745	0.04124	0.00292	0.00052	0.11053	0.03881	0.00259	0.00046

TABLE IX. v_2\{ZDC-SMD\} from S-N and ZDC-BBC-CNT subevents as a function of p_T in centralities 0–10%, 10–20%, and 20–30%.

Centrality $v_2\{\}$	p_T (GeV/c)	S-N subevents				ZDC-BBC-CNT subevents			
		v_2	σ_{stat}	σ^B_{syst}	σ^C_{syst}	v_2	σ_{stat}	σ^B_{syst}	σ^C_{syst}
	0.247	0.01342	0.00114	0.00013	0.00005	0.01723	0.00158	0.00022	0.00004
	0.348	0.01488	0.00131	0.00002	0.00007	0.01929	0.00183	0.00003	0.00005
	0.448	0.01231	0.00133	0.00002	0.00005	0.01688	0.00205	0.00003	0.00004
	0.548	0.02085	0.00170	0.00004	0.00013	0.02643	0.00230	0.00006	0.00010
	0.648	0.01557	0.00166	0.00002	0.00007	0.02132	0.00256	0.00003	0.00006
	0.748	0.02236	0.00203	0.00003	0.00015	0.02928	0.00289	0.00005	0.00012
	0.848	0.02656	0.00233	0.00003	0.00021	0.03444	0.00326	0.00005	0.00017
	0.948	0.03014	0.00265	0.00004	0.00027	0.03909	0.00371	0.00006	0.00021
	1.092	0.04275	0.00268	0.00006	0.00055	0.04922	0.00319	0.00008	0.00034
0–10%	1.292	0.03826	0.00304	0.00004	0.00044	0.04801	0.00405	0.00006	0.00032
v_2\{ZDC-SMD\}	1.492	0.03859	0.00367	0.00003	0.00045	0.05124	0.00534	0.00005	0.00037
	1.692	0.04492	0.00476	0.00005	0.00061	0.06137	0.00730	0.00009	0.00053
	1.892	0.06318	0.00654	0.00007	0.00120	0.08583	0.00992	0.00014	0.00103
	2.200	0.06910	0.00672	0.00006	0.00143	0.09233	0.00989	0.00011	0.00119
	2.703	0.07798	0.01123	0.00010	0.00182	0.11270	0.01925	0.00021	0.00178
	3.343	0.07481	0.01667	0.00018	0.00168	0.11230	0.03125	0.00041	0.00177
	0.247	0.02194	0.00061	0.00011	0.00006	0.02145	0.00067	0.00011	0.00003
	0.348	0.02987	0.00070	0.00008	0.00011	0.02924	0.00074	0.00008	0.00005
	0.448	0.03696	0.00078	0.00010	0.00017	0.03621	0.00083	0.00010	0.00008
	0.548	0.04342	0.00088	0.00015	0.00023	0.04255	0.00092	0.00014	0.00011
	0.648	0.05052	0.00098	0.00013	0.00031	0.04951	0.00103	0.00013	0.00016
	0.748	0.05556	0.00110	0.00013	0.00037	0.05445	0.00115	0.00012	0.00019
	0.848	0.06572	0.00125	0.00014	0.00052	0.06442	0.00130	0.00014	0.00026
	0.948	0.07064	0.00141	0.00014	0.00060	0.06923	0.00148	0.00014	0.00030
	1.092	0.07773	0.00122	0.00015	0.00073	0.07626	0.00126	0.00014	0.00037
10–20%	1.292	0.09169	0.00155	0.00016	0.00102	0.08993	0.00162	0.00015	0.00051
v_2\{ZDC-SMD\}	1.492	0.10236	0.00204	0.00019	0.00127	0.10031	0.00214	0.00019	0.00064
	1.692	0.11847	0.00275	0.00020	0.00170	0.11598	0.00293	0.00019	0.00085
	1.892	0.13255	0.00365	0.00029	0.00212	0.12960	0.00397	0.00028	0.00107
	2.200	0.13748	0.00363	0.00020	0.00229	0.13446	0.00393	0.00019	0.00115
	2.703	0.15166	0.00640	0.00022	0.00278	0.14772	0.00754	0.00021	0.00139
	3.343	0.14679	0.00945	0.00028	0.00261	0.14255	0.01196	0.00026	0.00129
	4.381	0.14874	0.02444	0.00064	0.00268	0.14410	0.03301	0.00060	0.00132
	5.410	0.02580	0.05846	0.00004	0.00008	0.02498	0.08004	0.00004	0.00004
	0.247	0.02479	0.00045	0.00035	0.00005	0.02523	0.00056	0.00037	0.00002
	0.348	0.03843	0.00052	0.00013	0.00011	0.03893	0.00061	0.00014	0.00005
	0.448	0.04673	0.00058	0.00013	0.00017	0.04726	0.00067	0.00013	0.00008
	0.548	0.05726	0.00065	0.00016	0.00025	0.05785	0.00075	0.00016	0.00012
	0.648	0.06796	0.00073	0.00017	0.00036	0.06860	0.00084	0.00018	0.00016
	0.748	0.07649	0.00082	0.00015	0.00045	0.07721	0.00094	0.00016	0.00021
	0.848	0.08664	0.00093	0.00018	0.00058	0.08745	0.00106	0.00018	0.00027
	0.948	0.09430	0.00105	0.00018	0.00069	0.09523	0.00120	0.00018	0.00032
	1.092	0.10554	0.00093	0.00019	0.00086	0.10622	0.00103	0.00020	0.00040
20–30%	1.292	0.12012	0.00118	0.00020	0.00112	0.12107	0.00132	0.00020	0.00051
v_2\{ZDC-SMD\}	1.492	0.13329	0.00153	0.00025	0.00138	0.13466	0.00176	0.00025	0.00064
	1.692	0.14589	0.00202	0.00026	0.00165	0.14785	0.00242	0.00026	0.00077
	1.892	0.16194	0.00265	0.00028	0.00204	0.16454	0.00327	0.00029	0.00095
	2.200	0.17353	0.00265	0.00028	0.00234	0.17613	0.00322	0.00029	0.00109
	2.703	0.18631	0.00458	0.00038	0.00269	0.19024	0.00610	0.00039	0.00127
	3.343	0.18180	0.00683	0.00042	0.00257	0.18612	0.00952	0.00044	0.00121
	4.381	0.17827	0.01783	0.00084	0.00247	0.18283	0.02570	0.00088	0.00117
	5.410	0.16731	0.04246	0.00184	0.00217	0.17163	0.06153	0.00194	0.00103

TABLE X. v_2\{ZDC-SMD\} from S-N and ZDC-BBC-CNT subevents as a function of p_T in centralities 30–40%, 40–50%, and 50–60%.

Centrality $v_2\{\}$	p_T (GeV/c)	S-N subevents				ZDC-BBC-CNT subevents			
		v_2	σ_{stat}	σ_{syst}^B	σ_{syst}^C	v_2	σ_{stat}	σ_{syst}^B	σ_{syst}^C
	0.247	0.02694	0.00045	0.00062	0.00004	0.02819	0.00061	0.00068	0.00002
	0.348	0.04133	0.00050	0.00014	0.00010	0.04305	0.00065	0.00015	0.00004
	0.448	0.05500	0.00057	0.00015	0.00018	0.05713	0.00071	0.00016	0.00007
	0.548	0.06605	0.00064	0.00013	0.00026	0.06852	0.00079	0.00014	0.00010
	0.648	0.07744	0.00073	0.00013	0.00035	0.08028	0.00089	0.00014	0.00013
	0.748	0.08648	0.00082	0.00016	0.00044	0.08966	0.00099	0.00017	0.00016
	0.848	0.09719	0.00092	0.00016	0.00055	0.10077	0.00112	0.00017	0.00021
	0.948	0.10647	0.00104	0.00014	0.00066	0.11046	0.00128	0.00016	0.00025
	1.092	0.12033	0.00093	0.00018	0.00085	0.12430	0.00110	0.00020	0.00031
30–40%	1.292	0.13425	0.00117	0.00015	0.00106	0.13898	0.00141	0.00017	0.00039
v_2\{ZDC-SMD\}	1.492	0.15041	0.00152	0.00025	0.00133	0.15615	0.00188	0.00027	0.00050
	1.692	0.16789	0.00203	0.00025	0.00165	0.17486	0.00260	0.00027	0.00062
	1.892	0.18310	0.00266	0.00031	0.00196	0.19124	0.00353	0.00033	0.00074
	2.200	0.18792	0.00263	0.00029	0.00207	0.19616	0.00346	0.00031	0.00078
	2.703	0.19298	0.00458	0.00033	0.00218	0.20250	0.00649	0.00036	0.00083
	3.343	0.19902	0.00685	0.00031	0.00232	0.20918	0.00995	0.00034	0.00089
	4.381	0.15951	0.01765	0.00077	0.00149	0.16787	0.02619	0.00085	0.00057
	5.410	0.03318	0.04176	0.00008	0.00006	0.03492	0.06213	0.00009	0.00002
	0.247	0.02601	0.00054	0.00060	0.00004	0.02771	0.00077	0.00068	0.00001
	0.348	0.04210	0.00060	0.00014	0.00010	0.04474	0.00081	0.00016	0.00003
	0.448	0.05541	0.00067	0.00012	0.00017	0.05880	0.00089	0.00013	0.00005
	0.548	0.06853	0.00076	0.00012	0.00026	0.07264	0.00099	0.00013	0.00008
	0.648	0.08077	0.00086	0.00011	0.00036	0.08558	0.00111	0.00013	0.00012
	0.748	0.09316	0.00097	0.00013	0.00048	0.09868	0.00125	0.00015	0.00015
	0.848	0.10257	0.00110	0.00015	0.00059	0.10868	0.00141	0.00017	0.00019
	0.948	0.11494	0.00125	0.00013	0.00074	0.12181	0.00161	0.00015	0.00023
	1.092	0.12842	0.00112	0.00012	0.00092	0.13572	0.00139	0.00014	0.00029
40–50%	1.292	0.14455	0.00141	0.00015	0.00116	0.15299	0.00179	0.00017	0.00037
v_2\{ZDC-SMD\}	1.492	0.15539	0.00183	0.00020	0.00134	0.16483	0.00240	0.00022	0.00043
	1.692	0.16641	0.00245	0.00023	0.00154	0.17691	0.00333	0.00027	0.00049
	1.892	0.18706	0.00325	0.00027	0.00195	0.19913	0.00453	0.00030	0.00063
	2.200	0.19007	0.00319	0.00025	0.00201	0.20228	0.00443	0.00028	0.00065
	2.703	0.19675	0.00563	0.00030	0.00215	0.20991	0.00824	0.00034	0.00069
	3.343	0.17518	0.00833	0.00043	0.00171	0.18706	0.01244	0.00049	0.00055
	4.381	0.15207	0.02120	0.00062	0.00129	0.16245	0.03198	0.00071	0.00042
	5.410	0.23778	0.04958	0.00360	0.00315	0.25402	0.07485	0.00410	0.00102
	0.247	0.02164	0.00071	0.00034	0.00004	0.02529	0.00114	0.00047	0.00002
	0.348	0.03766	0.00077	0.00013	0.00011	0.04384	0.00120	0.00017	0.00007
	0.448	0.05159	0.00087	0.00013	0.00021	0.05986	0.00132	0.00017	0.00013
	0.548	0.06277	0.00098	0.00010	0.00031	0.07273	0.00148	0.00013	0.00020
	0.648	0.07471	0.00111	0.00009	0.00044	0.08647	0.00166	0.00012	0.00028
	0.748	0.08320	0.00125	0.00009	0.00054	0.09633	0.00188	0.00012	0.00035
	0.848	0.09675	0.00143	0.00015	0.00074	0.11196	0.00214	0.00020	0.00047
	0.948	0.10720	0.00163	0.00008	0.00090	0.12413	0.00244	0.00011	0.00058
	1.092	0.11901	0.00146	0.00010	0.00111	0.13707	0.00212	0.00013	0.00070
50–60%	1.292	0.12717	0.00184	0.00013	0.00127	0.14709	0.00274	0.00017	0.00081
v_2\{ZDC-SMD\}	1.492	0.14188	0.00243	0.00019	0.00158	0.16469	0.00370	0.00025	0.00101
	1.692	0.15811	0.00331	0.00021	0.00196	0.18411	0.00516	0.00028	0.00127
	1.892	0.15997	0.00439	0.00035	0.00201	0.18679	0.00701	0.00048	0.00131
	2.200	0.16724	0.00431	0.00037	0.00220	0.19518	0.00684	0.00051	0.00142
	2.703	0.18027	0.00776	0.00047	0.00255	0.21100	0.01265	0.00064	0.00166
	3.343	0.13888	0.01139	0.00041	0.00152	0.16274	0.01878	0.00056	0.00099
	4.381	0.12204	0.02867	0.00202	0.00117	0.14306	0.04745	0.00277	0.00077

[1] I. Arsene *et al.* (BRAHMS Collaboration), Nucl. Phys. **A757**, 1 (2005).
[2] K. Adcox *et al.* (PHENIX Collaboration), Nucl. Phys. **A757**, 184 (2005).
[3] B. B. Back *et al.* (PHOBOS Collaboration), Nucl. Phys. **A757**, 28 (2005).
[4] J. Adams *et al.* (STAR Collaboration), Nucl. Phys. **A757**, 102 (2005).
[5] M. Gyulassy and L. McLerran, Nucl. Phys. **A750**, 30 (2005).
[6] B. Muller, arXiv:nucl-th/0404015.
[7] E. V. Shuryak, Nucl. Phys. **A750**, 64 (2005).
[8] J.-Y. Ollitrault, Phys. Rev. D **46**, 229 (1992).
[9] P. F. Kolb, U. W. Heinz, P. Huovinen, K. J. Eskola, and K. Tuominen, Nucl. Phys. **A696**, 197 (2001).
[10] T. Hirano and Y. Nara, Nucl. Phys. **A743**, 305 (2004).
[11] N. N. Ajitanand (PHENIX Collaboration), Nucl. Phys. **A715**, 765 (2003).
[12] M. Chiu (PHENIX Collaboration), Nucl. Phys. **A715**, 761 (2003).
[13] C. Adler *et al.* (STAR Collaboration), Phys. Rev. Lett. **90**, 082302 (2003).
[14] S. S. Adler *et al.* (PHENIX Collaboration), Phys. Rev. C **71**, 051902 (2005).
[15] J. Adams *et al.* (STAR Collaboration), Phys. Rev. Lett. **95**, 152301 (2005).
[16] S. S. Adler *et al.* (PHENIX Collaboration), Phys. Rev. Lett. **97**, 052301 (2006).
[17] A. Adare *et al.* (PHENIX Collaboration), Phys. Rev. C **78**, 014901 (2008).
[18] M. Bleicher and H. Stoecker, Phys. Lett. **B526**, 309 (2002).
[19] S. S. Adler *et al.* (PHENIX Collaboration), Phys. Rev. Lett. **91**, 182301 (2003).
[20] Z. Xu, C. Greiner, and H. Stocker, J. Phys. G **35**, 104016 (2008).
[21] J. Adams *et al.* (STAR Collaboration), Phys. Rev. Lett. **92**, 052302 (2004).
[22] A. Adare *et al.* (PHENIX Collaboration), Phys. Rev. Lett. **98**, 162301 (2007).
[23] S. Huang (PHENIX Collaboration), J. Phys. G **35**, 104105 (2008).
[24] D. Molnár and S. A. Voloshin, Phys. Rev. Lett. **91**, 092301 (2003).
[25] R. J. Fries, B. Müller, C. Nonaka, and S. A. Bass, Phys. Rev. C **68**, 044902 (2003).
[26] V. Greco, C. M. Ko, and P. Lévai, Phys. Rev. C **68**, 034904 (2003).
[27] A. Shor, Phys. Rev. Lett. **54**, 1122 (1985).
[28] A. M. Poskanzer and S. A. Voloshin, Phys. Rev. C **58**, 1671 (1998).
[29] J. Jia (PHENIX Collaboration), Nucl. Phys. **A783**, 501 (2007).
[30] J. Putschke, J. Phys. G **34**, S679 (2007).
[31] B. Alver *et al.* (PHOBOS Collaboration), arXiv:0903.2811.
[32] P. Sorensen (STAR Collaboration), J. Phys. G **35**, 104102 (2008).
[33] M. Miller and R. Snellings, arXiv:nucl-ex/0312008.
[34] J.-Y. Ollitrault, A. M. Poskanzer, and S. A. Voloshin, Phys. Rev. C **80**, 014904 (2009).
[35] K. Adcox *et al.* (PHENIX Collaboration), Nucl. Instrum. Methods A **499**, 469 (2003).
[36] M. Allen *et al.* (PHENIX Collaboration), Nucl. Instrum. Methods A **499**, 549 (2003).
[37] C. Adler *et al.*, Nucl. Instrum. Methods A **499**, 433 (2003).
[38] M. L. Miller, K. Reygers, S. J. Sanders, and P. Steinberg, Annu. Rev. Nucl. Part. Sci. **57**, 205 (2007).
[39] R. J. Glauber and G. Matthiae, Nucl. Phys. **B21**, 135 (1970).
[40] K. Adcox *et al.* (PHENIX Collaboration), Phys. Rev. Lett. **86**, 3500 (2001).
[41] S. S. Adler *et al.* (PHENIX Collaboration), Phys. Rev. C **69**, 034910 (2004).
[42] J. T. Mitchell *et al.* (PHENIX Collaboration), Nucl. Instrum. Methods A **482**, 491 (2002).
[43] S. S. Adler *et al.* (PHENIX Collaboration), Phys. Rev. C **73**, 054903 (2006).
[44] N. Borghini, P. M. Dinh, and J.-Y. Ollitrault, Phys. Rev. C **64**, 054901 (2001).
[45] N. Borghini, P. M. Dinh, and J.-Y. Ollitrault, arXiv:nucl-ex/0110016.
[46] C. Alt *et al.* (NA49 Collaboration), Phys. Rev. C **68**, 034903 (2003).
[47] C. Adler *et al.* (STAR Collaboration), Phys. Rev. C **66**, 034904 (2002).
[48] I. Selyuzhenkov and S. Voloshin, Phys. Rev. C **77**, 034904 (2008).
[49] J. Adams *et al.* (STAR Collaboration), Phys. Rev. C **72**, 014904 (2005).
[50] B. Alver *et al.* (PHOBOS Collaboration), Phys. Rev. Lett. **98**, 242302 (2007).
[51] J. Adams *et al.* (STAR Collaboration), Phys. Rev. Lett. **93**, 252301 (2004).
[52] R. S. Bhalerao and J.-Y. Ollitrault, Phys. Lett. **B641**, 260 (2006).